

A nanoporous capacitive electrochemical ratchet for continuous ion separations

Rylan J. Kautz¹, Alon Herman², Ethan J. Heffernan¹, Camila Muñetón^{3,4}, David Larson^{5,6}, Joel W. Ager III^{5,6,7,8}, Francesca M. Toma^{5,6}, Shane Ardo^{1,3,9*} and Gideon Segev^{2,5,6**}

¹Department of Materials Science & Engineering, University of California, Irvine, CA 92697, USA

²School of Electrical Engineering, Tel Aviv University, Tel Aviv 6997801, Israel

³Department of Chemistry, University of California, Irvine, CA 92697, USA

⁴Department of Chemistry, University of Massachusetts, Boston, MA 02125 USA

⁵Chemical Sciences Division, Lawrence Berkeley National Lab, Berkeley, CA 94720, USA

⁶Joint Center for Artificial Photosynthesis, Lawrence Berkeley National Lab, Berkeley, CA 94720, USA

⁷Materials Sciences Division, Lawrence Berkeley National Lab, Berkeley, CA 94720, USA

⁸Department of Materials Science and Engineering, University of California Berkeley, CA 94720, USA

⁹Department of Chemical & Biomolecular Engineering, University of California, Irvine, CA 92697, USA

*Email: ardo@uci.edu

**Email: gideons1@tauex.tau.ac.il

Summary

Directed ion transport in liquid electrolyte solutions underlies numerous phenomena in nature and industry including neuronal signaling, photosynthesis and respiration, electrodialysis for desalination, and recovery of critical materials.¹⁻⁶ Here, we report the first demonstration of an ion pump that drives ions in aqueous electrolytes against a force using a capacitive ratchet mechanism. Our ratchet-based ion pumps utilize the non-linear capacitive nature of electric double layers for symmetry breaking which drives a net time-averaged ion flux in response to a time varying input signal. Since the devices are driven by a non-linear charging and discharging of double layers, they do not require redox reactions for continual operation. Ratchet-based ion pumps were fabricated by depositing thin gold layers on the two surfaces of anodized alumina wafers, forming nanoporous capacitor-like structures. Pumping occurs when a wafer is placed between two compartments of aqueous electrolyte and the electric potential across it is modulated. In response to various input signals, persistent ionic voltages and sustained currents were observed, consistent with net unidirectional ion transport, even though conduction through the membrane was non-rectifying. The generated ionic power was used in conjunction with an additional shunt pathway to demonstrate electrolyte demixing.

The Ratchet-Based Ion Pump

Ratchets are non-equilibrium devices that utilize temporally modulated input signals and spatial asymmetries to drive a steady state particle flux.⁷⁻⁹ Ratchets of various types have been studied both theoretically and experimentally⁸⁻¹³ for electronic signal rectification,⁷⁻¹⁶ to drive net transport of uncharged species through induced charge electrokinetics,¹⁷ micro and nanoparticle sorting,¹⁸⁻²⁵ and to drive net ionic current and pump water by alternating redox reactions.²⁶⁻²⁸ Here we demonstrate for the

first time an electrochemical device driven with a capacitive ratchet mechanism. The fabricated devices drive sustained direct ionic currents against a force without invoking Faradaic redox reactions. Therefore, these devices potentially enable continuous desalination using a modular, small-scale device architecture powered only by electricity and with no moving parts. Furthermore, utilizing the sorting properties of ratchets,^{18–25,29} ratchet based ion pumps (RBIPs) may pave the way toward a long sought after selective ion separation technology.^{4–6}

The double layer capacitance between an electrolyte and a blocking electrode (an electrode where no faradaic reactions take place) varies with the magnitude of the electric potential and in response to temporal changes in it.^{30–32} As a result, the time constants for charging and discharging the double layer change as a function of the electrical signals that are applied to the electrode. Here we utilize this phenomenon to pump ions across a membrane. Figure 1a shows a schematic illustration of the operating principles of the RBIP. The RBIPs are made of nanoporous anodized aluminum oxide (AAO) wafers with thin metal layers that cover the two surfaces of the wafers without blocking the pores, thus forming nanoporous capacitor-like structures that could be wetted by aqueous electrolyte. The effective time constants for charging and discharging the double layers on each side of the RBIP are determined by the effective impedance between the metal layers and the bulk solution (Z_L , Z_R for left and right surfaces, respectively, in Figure 1a), and the impedances between the metal layers and the electrolyte within the pore ($Z_{L,p}$ and $Z_{R,p}$ in Figure 1a). When an input signal, V_{in} , is applied between the two metal layers, the double layer at one surface is charged while the other is discharged with time constants that are determined by the properties of the input signal and the metal surface. The potential difference between the bulk solution and the adjacent metal surface at each side of the RBIP (V_L and V_R in Figure 1a) fluctuates according to these time constants. According to the notations in Figure 1a, the electric potential difference between the bulk of the two electrolyte compartments is:

$$V_{out}(t) = V_L(t) + V_{in}(t) - V_R(t) \quad (1)$$

In equation (1) V_R has an opposite polarity because the potential differences V_L and V_R are defined with respect to the electrostatic potential in the bulk solution of each compartment. In the subsequent sections we show that if the charge and discharge time constants are different, a net time-averaged electric potential difference, \bar{V}_{out} , develops between the two electrolyte compartments. This potential difference provides a driving force for ion transport from one side of the membrane to the other.

Experimental demonstration

RBIPs were fabricated using several processes, all showing similar results (see details in methods section). Figure 1b,c show a plan view and a cross-section SEM images, respectively, of two RBIPs. Figure 1d shows a photograph of a sample before its assembly inside an electrochemical cell. Figure S1 shows an illustration of this sample and cell. The RBIPs performance was tested by placing an RBIP between two compartments of chloride containing electrolyte and measuring the voltage between two Ag/AgCl wires, which are immersed in the solution on each side of the RBIP (V_{out}). The voltage V_L was measured between the left gold contact and the adjacent Ag/AgCl wire, and V_R was calculated using equation (1). Figure 1e shows a photograph of the RBIP performance characterization setup.

Because of the extremely high reaction rate of Cl^- with the Ag/AgCl wires, the voltage difference between the two Ag/AgCl wires is the electrochemical potential difference for chlorides. Hence, \bar{V}_{out} is the net driving force for chloride transport from one compartment to the other. The measured resting voltage between the two Ag/AgCl wires, V_{rest} , when both compartments are filled with the same electrolyte (1 –

10 mM Cl⁻ containing solution) is lower than 10 mV and is typically about 2-3 mV. Application of a DC bias across the Au contacts of the RBIP (V_{in} of +300 mV or -300 mV) resulted in the expected prompt observation of $V_{out} \approx V_{in}$ that decayed to $V_{out} \approx V_{rest}$ over ~1 sec due to capacitive charging. Hence, under these conditions there is no steady state net driving force for Cl⁻ flow through the RBIP.

To demonstrate the difference in charging and discharging time constants and their contribution to \bar{V}_{out} , the voltage signals $V_L(t)$ and $V_R(t)$ were measured while the RBIP was operating. The input signal was a rectangular wave in the form:

$$V_{in}(t) = \begin{cases} V_a & 0 < t \leq d_c T \\ -V_a & d_c T < t \leq T \end{cases} \quad (2)$$

where T is the time period and d_c ($\in [0,1]$) is the duty cycle.

Figure 1f-g shows V_L and V_R , respectively. The input signal amplitude, V_a , is 0.3 V and the frequency ($= 1/T$) is 20 Hz. The RBIP pore diameter is 60 nm, and the electrolyte is 1 mM KCl in aqueous solution. The color coding for both V_L and V_R marks the duty cycle of the input signal. The dots are the average signals calculated by obtaining the mean responses out of 300 periods. The voltages measured within the time interval $0 < t \leq d_c T$ (green background in Figure 1f-g) are denoted with a subscript 1, and the voltages within the time interval $d_c T < t \leq T$ (red background in Figure 1f-g) are denoted with a subscript 2. In the subsequent discussion, the terms charging/discharging are used to describe an increase/decrease in voltage over time (in absolute value). Because the RBIP is electrically floating (i.e., no part of the system is grounded), charging of one contact is accompanied by discharging of the other. For example, for $0 < t \leq d_c T$, the signal $V_{L,1}$ shows a discharging trend, and $V_{R,1}$ is charging. In a similar manner, for $d_c T < t \leq T$, while $V_{L,2}$ is charging, $V_{R,2}$ is discharging. To find the charging and discharging time constants of every surface at every part of the period, the averaged signals were fitted to a single exponential charging/discharging function:

$$V(t) = V_f + (V_i - V_f) \exp\left(-\frac{t}{\tau}\right) \quad (3)$$

where V_i is initial voltage, and τ is the time constant for charging or discharging the surface. V_f is the voltage at which the signal would saturate if the capacitances were linear. The solid lines in Figure 1f-g are the fitted curves. Figure 1h shows the extracted time constants for charging and discharging of the two surfaces as a function of the duty cycle. The error bars indicate the fitting 95% confidence interval. All time constants vary with the duty cycle demonstrating a significant capacitance frequency dispersion. For duty cycles above 0.4 the time constants of the two surfaces are similar yet vary significantly between the first part and the second part of the period: $\tau_{L,1} \approx \tau_{R,1} \neq \tau_{L,2} \approx \tau_{R,2}$. Furthermore, the time constants, $\tau_{R,1}$ and $\tau_{R,2}$ are nearly mirror images of each other with respect to a duty cycle of 0.5: $\tau_{R,1}(d_c) \approx \tau_{R,2}(1 - d_c)$. The only data points that deviate from this trend are the time constants for the left interface at the first two duty cycles studied. A similar analysis for signals with different frequencies at a duty cycle of 0.5 shows that all the time constants decrease significantly with the signal frequency (Figure S2-3). Thus, the charging and discharging dynamics are mostly determined by the duration for charging and discharging the surfaces. As a result, the difference in the charging and discharging time constants is smallest for a duty cycle of 0.5 and for this duty cycle it is determined by the non-linear nature of the capacitance with the potential.

\bar{V}_{out} was then obtained by finding the mean value of V_{out} while the ratchet is ON and reducing from it the mean value of V_{out} while the ratchet was OFF (see the methods section for more details). Figure 1i shows

the measured \bar{V}_{out} as a function of the input signal duty cycle. As in other demonstrations of ratchets,^{7,10} the RBIP output is very low when a constant bias is applied (duty cycle of 0 or 1). However, once the input signal is alternating, a net voltage builds up between the two compartments providing a driving force for ion transport. The sign of \bar{V}_{out} does not change with the duty cycle, which is similar to a flashing ratchet in an ON-OFF mode of operation.⁷ Since the charging and discharging dynamics of the two surfaces are different (Figure 1h), the potential distribution through the pores fluctuates asymmetrically even when an unbiased input signal ($d_c = 0.5$) is applied. Temporal fluctuation of an asymmetric potential distribution is the basic mechanism behind charge transport in flashing ratchets.³³ An analysis of our devices in terms of flashing ratchet principles is left for future work.

The charging/discharging response to a large voltage step is non-linear with the potential.³⁴ As a result, the time constants describing the charging and discharging of the surfaces increase with the duration of the voltage step. For example, the fitted curves in Figure 1 f-g consistently underestimate the temporal change near $t=0$ and $t=d_c T$. Conversely, the voltages V_L and V_R do not saturate at $\pm V_a/2$ for voltage steps with durations that are longer than the time constants in Figure 1h, and the fitted steady state voltage V_f decreases with the input signal frequency (Figure S3). Hence, at high frequencies the voltage V_L and V_R alternate according to an effective input signal with an amplitude that is smaller than V_a , potentially reducing the output of the device.

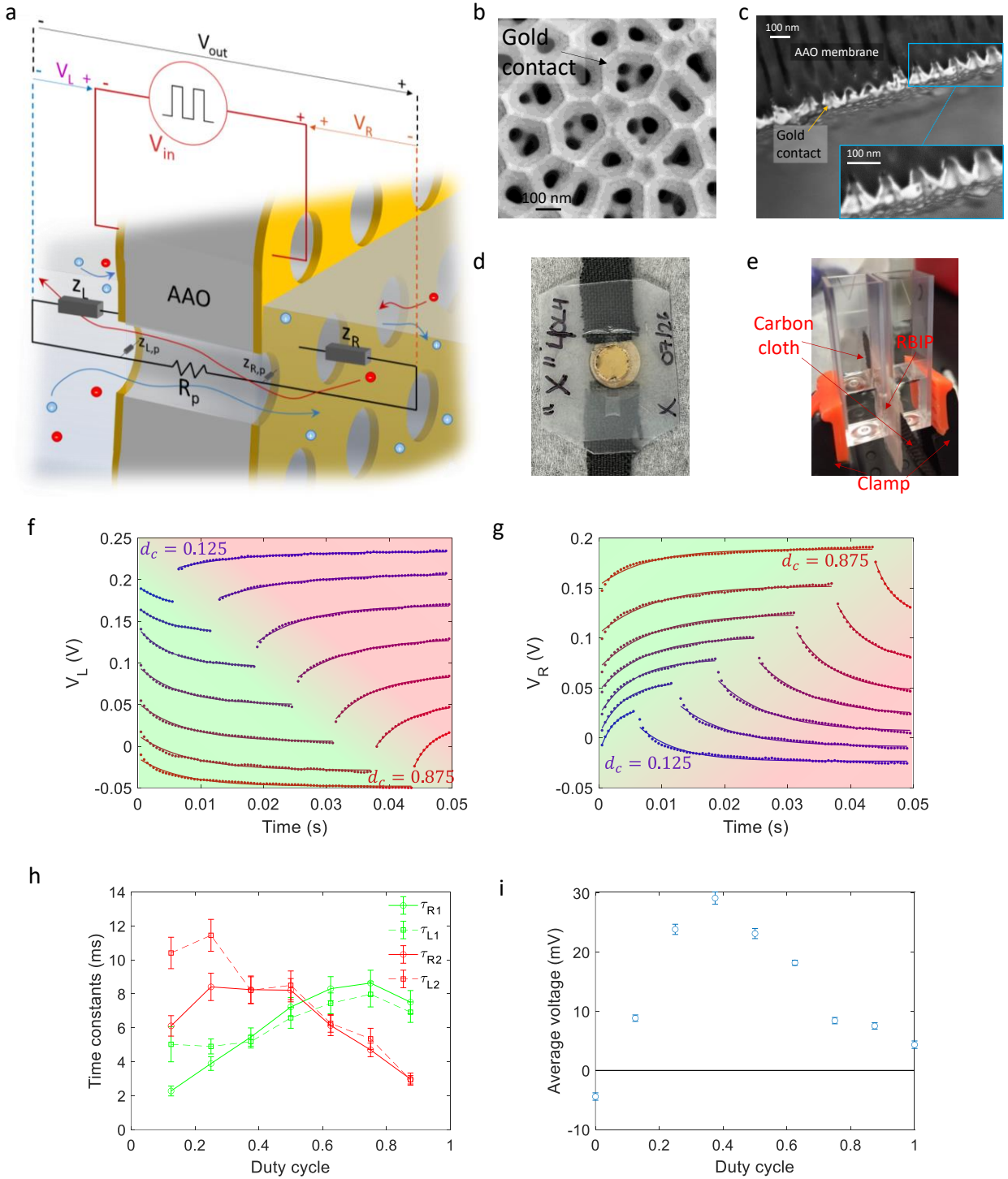


Figure 1: The RBIP|(a) A schematic illustration of the RBIP structure and double layers impedances. (b-c) Plan and cross section view SEM images of fabricated RBIPs respectively. (d-e) Experimentally measured signals $V_L(t)$ and $V_R(t)$, respectively, for rectangular-wave inputs with various duty cycles, d_c , and a period, T , of 50 ms. The green areas are for the first portion of the period $0 < t \leq d_c T$ and the red areas are for the second portion of the period $d_c T < t \leq T$. The dots are the measurements, and the solid lines mark the best exponential fit to the data. The color coding marks the duty cycle and is the same in both (f) and (g). (h) Time constants extracted from the fitted curves in (f) and (g). Subscripts 1 and 2 denote that the time constants were extracted for the first ($0 < t \leq d_c T$) and second ($d_c T < t \leq T$) part of the input signal, respectively. (i) The time averaged output voltage

\bar{V}_{out} as a function of the input signal duty cycle. The electrolyte is 1 mM KCl aqueous solution and the input signal is alternating between 300 mV and -300 mV at a frequency of 20 Hz.

Next, we measured the ratchet performance and extracted the charging and discharging time constants for input signals with various frequencies and duty cycles. The RBIP pore diameter is 40 nm, the input signal amplitude V_a is 0.3 V and the solution is 1 mM HCl aqueous solution. Figure 2a shows the average temporal response V_{out} at a duty cycle of 0.5 and several frequencies. The time for each signal was normalized by its period. The average response was obtained by averaging several periods as described in the methods section. The response for other duty cycles and the best fit to exponential functions are shown in supporting figure S4. Figure 2b shows the time constants extracted from V_{out} for the two parts of the input signal period as a function of the duty cycle and frequency. The color coding marks the signal frequency and it is as in Figure 2a. Similar to the trends observed in Figure 1h, the time constants for $0 < t \leq d_c T$ are an almost perfect mirror image of the time constants at $d_c T < t \leq T$. Furthermore, the time constants drop significantly with the input signal frequency. Figure 2c shows the net output voltage \bar{V}_{out} as a function of the duty cycle and frequency. As in Figure 1i, here also the output is practically zero for extreme duty cycles and low frequencies when the device is effectively at its steady state for significant parts of the temporal period. The output voltage increases with the input signal frequency reaching about -17 mV at a frequency of 250 Hz and duty cycle of 0.6. Although the RBIP output increases with frequency within this range, it decreases for higher frequencies (Figure S7 and Figure S10).

\bar{V}_{out} values for an aqueous 1 mM electrolyte were observed to be larger than \bar{V}_{out} values for an aqueous 10 mM electrolyte (Figure S7). Since the resistance for charge transport through the pore, R_p effectively shunts \bar{V}_{out} (Figure 1a), solutions with high ionic strength and membranes with a large pore diameter will tend to produce a lower RBIP output. The ionic strength of the solution also affects the double layer capacitances and the charging and discharging time constants at the RBIP surfaces leading to higher optimal frequencies (Figure S7). A detailed analysis of the contribution of this effect to \bar{V}_{out} is left to future work. We observed that the diminished performance with higher concentration solutions can be partially mitigated with the use of AAO membranes with smaller pores, but at the expense of higher overall ionic resistance per pore (Figure S10). Ratcheting was also demonstrated with \bar{V}_{out} measured between two leak-free reference electrodes, decoupling between the electric potential and chemical potential induced by the ratchet (Figure S9a,b). More details on the measurement of \bar{V}_{out} and \bar{I}_{out} and the output dependence on different input signals and solution parameters can be found in the supporting information.

The buildup of \bar{V}_{out} results in the separation of cations and anions until columbic forces negate the ratchet action preventing further charge transport. Hence, to drive a sustained net ionic current, charge neutrality must be maintained. This can be obtained by shorting the two Ag/AgCl wires thus providing a low resistance path for removing chlorides from one compartment and generating them in the other. In this case, the current between the Ag/AgCl wires, I_{out} , is a result of oxidation of one silver wire to silver chloride, and reduction of silver chloride on the other wire to form silver and an aqueous chloride. The generation of chlorides in one compartment and their removal in the other balances deviations from electroneutrality due to ion pumping driven by the charging and discharging of the RBIP contacts. Thus, I_{out} is approximately the difference between the cation and anion fluxes through the RBIP. Figure 2c shows the net current density output \bar{I}_{out}/A as a function of the input signal duty cycle and frequency. As for the voltage output, the current output shows a ratchet-like behavior with zero net output current at duty cycles of 0 and 1. However, once an alternating input signal is injected to the device, a significant

output current flows reaching as much as $3.15 \mu\text{A}/\text{cm}^2$ at a frequency of 250 Hz and duty cycle of 0.6. Figure S5a show the average temporal response for a duty cycle of 50% and the Figure S5b shows extracted time constants for all frequencies and duty cycles.

To demonstrate the ratchet driving ions against a force, a current-voltage scan was taken between the two Ag/AgCl wires while the ratchet is OFF ($V_{in} = 0 \text{ V}$) and when it was ON with a duty cycle of 50% and a frequency of 100 Hz. All other ratchet and signal parameters are as above. Figure 2g shows the current density \bar{I}_{out}/A as a function of \bar{V}_{out} . When the ratchet is OFF, the curve shows an expected linear ohmic behavior. This is in contrast to membranes with conical nano-pores that were shown to have a rectifying transport behavior.^{26,27} However, when the ratchet is ON, the curve shifts by the \bar{V}_{out} value determined by the input signal characteristics thus entering a quadrant in which ions are driven against an electrostatic force. Since the current voltage curve is linear, the energetic efficiency of the RBIP is approximately $\eta = 0.25V_{oc}I_{sc}/\bar{P}_{in}$ where V_{oc} and I_{sc} are the open circuit voltage and the short circuit current as shown in Figure 2c,f respectively and \bar{P}_{in} is the time averaged input power. At a frequency of 250 Hz and a duty cycle of 50%, the input power is approximately 0.215 mW which with the corresponding output from Figure 2c,f results in an efficiency of about $1.96 \cdot 10^{-5}$.

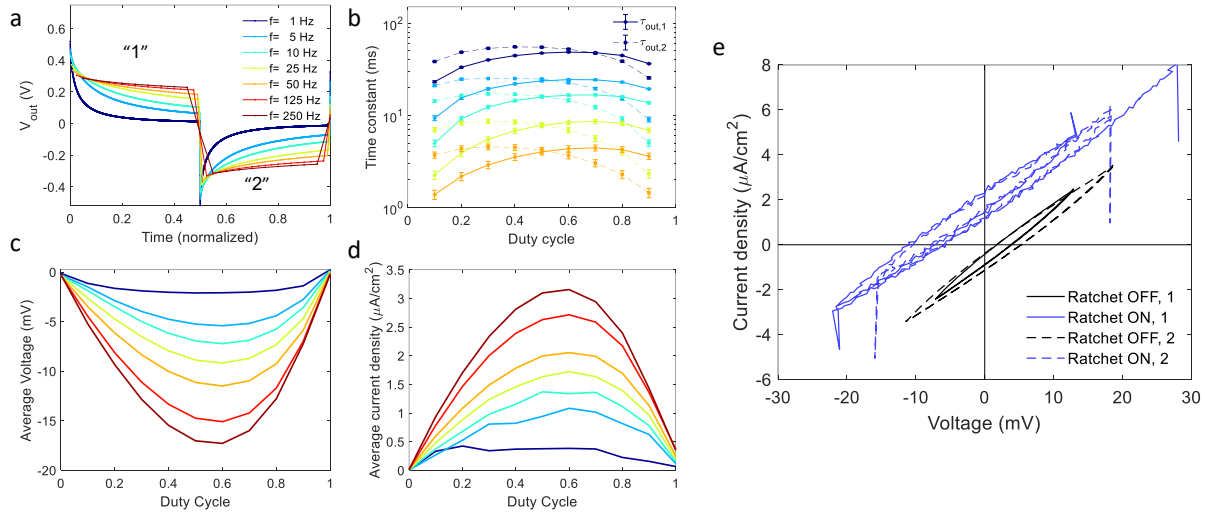


Figure 2: RBIP performance examination (a) V_{out} as a function of time for several input signal frequencies and a duty cycle of 0.5. (b) the time constants of V_{out} for several input signal frequencies and duty cycles. (c) \bar{V}_{out} as a function of the input signal duty cycle frequency. (d) The current density, I_{out}/A , as a function of time for several input signal frequencies and a duty cycle of 0.5. (e) the time constants of I_{out} for several input signal frequencies and duty cycles. (f) the time averaged current density \bar{I}_{out}/A as a function of the input signal duty cycle and frequency. The color coding for the input signal frequency is as (a) and (d). (g) Current-Voltage curves (\bar{I}_{out}/A , \bar{V}_{out}) with $V_{in} = 0$ and with a square-wave input at 50% duty cycle and 100 Hz frequency. In all these measurements the solution is 1 mM HCl aqueous solution, the RBIP pore diameter is 40 nm, the active area of the membrane is $A = 0.32 \text{ cm}^2$, and the input signal amplitude, V_a is 0.3 V.

As discussed above, for a significant concentration gradient to develop, charge neutrality must be maintained within the two compartments. This can be achieved by driving the ratchet while two Ag/AgCl auxiliary electrodes are shunted across the RBIP to provide a low-impedance pathway for electronic current to flow and an ample capacity of solid AgCl. Figure 3a shows a schematic illustration of such a system. By removing Cl^- from the solution through oxidation at one auxiliary electrode and generating Cl^- on the other, the shorted auxiliary electrodes assure that charge neutrality is maintained regardless of differences in ratchet-induced chloride and cation currents. Thus, when cations are pumped by the RBIP

into one compartment, chlorides are generated there to compensate for any additional positive charge, leading to an increase in electrolyte concentration. At the same time, since cations leave the other compartment and chlorides are removed through the auxiliary electrode, the electrolyte in this compartment is diluted. Thus, as the ratchet is turned ON, the current \bar{I}_{out} is composed of two contributions: the chloride current induced by the ratchet, and the generation and removal of chlorides required to compensate for the cation transport across the RBIP. Since the magnitude of the latter current component is determined by the net cation flux through the ratchet, it can be increased by choosing a cation with a high diffusion coefficient, for example protons in an HCl solution. As the cation concentration builds in one compartment and decreases in the other, it impedes further cation transport. After a sufficiently long time, the force exerted by the ratchet will be equal to the force induced by the concentration gradient and cations will no longer be transported through the RBIP. At this stage \bar{I}_{out} will be at a magnitude that supports the ratchet induced current and back diffusion without violating electroneutrality in either compartment.

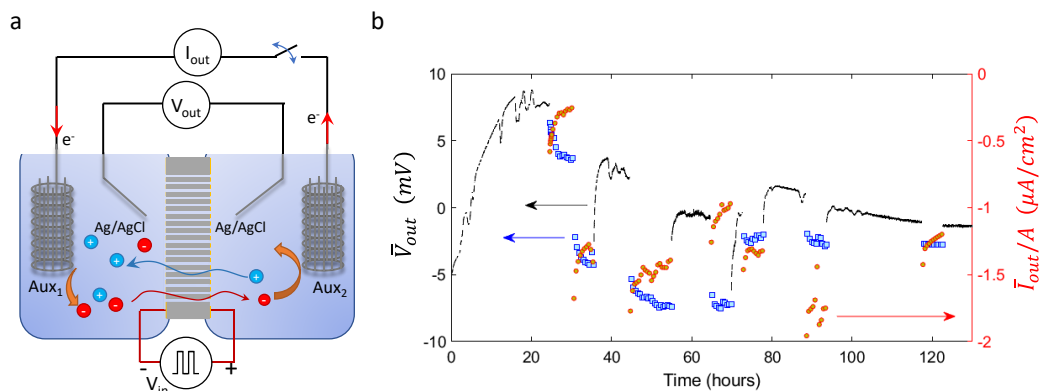


Figure 3: demixing demonstration | (a) Schematic illustration of an electrochemical cell used to demonstrate electrolyte demixing. (b) The voltage difference between two Ag/AgCl wires measured while the ratchet is OFF between periods of ratchet operation (blue) and while the system is continuously at rest (black). The red markers are the average current density measured between the Ag/AgCl meshes during every ratchet ON period. The input signal is a rectangular wave with duty cycle of 0.5, frequency of 125 Hz and an amplitude, V_o , of 0.3 V. The solution is 1 mM HCl aqueous solution, the RBIP pore diameter is 40 nm, the active area of the membrane is $A = 0.32 \text{ cm}^2$.

RBIP-driven electrolyte demixing was demonstrated with a system as illustrated in Figure 3a. Two Ag/AgCl wire meshes were used as auxiliary electrodes, and a set of Ag/AgCl wires was used to measure the chloride electrochemical potential difference between the two compartments. The RBIP sample had the same parameters as the one discussed in Figure 2 and the input signal was a square wave with duty cycle of 0.5, frequency of 125 Hz and an amplitude, V_a , of 0.3 V. The output of this sample is shown in Figure S11a-b. Figure 3b shows the measured voltage for several periods of operation measured over the course of 5 days. For the first 24 hours the system was at rest ($V_{in} = 0 \text{ V}$) allowing it to equilibrate. Then, to demonstrate demixing, the RBIP was operated continuously with the auxiliary electrodes shunted, thus concentrating the solution in one compartment and diluting solution in the other as described above. Next, the ratchet was turned OFF for 30 to 90 seconds and the voltage between the Ag/AgCl wires was measured. The current was not measured while the ratchet was OFF, thus the auxiliary electrodes were not shunted during this period (illustrated by the opening of the switch in Figure 3a). This process was repeated for multiple cycles as described in the methods section. The blue markers in Figure 3b mark the average voltage within each OFF period. The red markers are the average current (normalized by the RBIP

active area) measured between the two Ag/AgCl meshes while the ratchet is ON. After several hours of operation, V_{in} was set to 0 V for several hours and the system was allowed to equilibrate (black curves in Figure 3b). The slow drift in voltage observed while the system is at rest is attributed to slow changes in the Ag/AgCl wires. When the cell was allowed to equilibrate with $V_{in} = 0$ V over the course of at least one day, it attained an exceptionally stable and low voltage. However, following ratchet operation, a non-negligible and consistent offset of \bar{V}_{out} is observed demonstrating electrolyte demixing. The current induced by the ratchet operation is consistent with the sign of the drop in voltage after ratchet operation. Since electroneutrality was maintained throughout the experiment, and the voltage was measured within a time interval that is sufficient for discharging the RBIP capacitances, but too short to support complete back diffusion of ions, the measured voltage is determined by the chemical potential difference for chlorides between the two compartments, $\Delta\mu^{Cl^-}$, and the electrostatic potential difference induced by the RBIP permselectivity.³⁵ Both components are a result of a concentration difference between the two compartments, hence the measured voltage is indicative of ratchet driven demixing. The correlation between the concentration ratio and the measured voltage was calibrated by measuring the voltage between the two compartments with various concentration ratios. The calibration curve obtained with these measurements is shown in Figure S13. Using this correlation, and the voltage difference between periods of ratchet operation and when the system is at rest (about -7 mV), results in a concentration ratio of about 0.78. Over the course of the week, the output of the ratchet was reduced due to sample degradation. Further discussion of device degradation and other failure modes can be found in the supporting information.

Device simulation

The ratchet performance can be simulated by assuming that the voltages V_L and V_R follow a charging and discharging behavior as in equation (3), and inserting them and the input signal into equation (1). The non-linear nature of the double layer impedances is approximated by assigning different time constants for the surfaces charging and discharging. Since these time constants are determined mostly by the duration of the charging and discharging period, and the devices are nearly symmetric (**Figure 1h**, **Figure 2b,e**) it can be assumed that $\tau_{l,2} = \tau_{r,2}$ and $\tau_{l,1} = \tau_{r,1}$. \bar{V}_{out} was calculated using this procedure for various input signals and time constants. More details on the computational model can be found in the supporting information. Figure 4a shows the normalized output, \bar{V}_{out}/V_a , as a function of the duty cycle for several input signal frequencies. The charging and discharging time constants are $\tau_{L,2} = \tau_{R,2} = 2$ ms, $\tau_{L,1} = \tau_{R,1} = 8$ ms which are close to those extracted from experiment (**Figure 1h**). The amplitude of the input signal is $V_a = 0.3$ V. The output curves show a ratchet-like behavior with outputs near zero for extreme duty cycles and temporal periods that are significantly longer than the charging and discharging time constants. Like the experimental results, the output reaches a maximum at moderate duty cycles and higher frequencies. Figure 4b shows similar curves for $\tau_{L,2} = \tau_{R,2} = 1$ ms, $\tau_{L,1} = \tau_{R,1} = 100$ ms. For such extreme time constants, the output is higher and the optimal duty cycle shifts toward 1. In both cases, the output saturates when increasing the frequency. Figure 4c shows the maximal normalized output (in terms of absolute values) as a function of $\tau_{R,1}$ and $\tau_{R,2}$, with $\tau_{L,1} = \tau_{R,1}$ and $\tau_{L,2} = \tau_{R,2}$. Figure 4d shows the optimal duty cycle for every set of time constants. The parameters used in Figure 4a,b are marked with a triangle and a diamond respectively. When the RBIP capacitance is linear, i.e. all the time constants are equal, the output is 0. However, the output increases with the difference in time constants reaching values that approach $2V_a$ (in absolute value) at optimal duty cycles that shift toward 0 or 1 for very large differences between the time constants. Hence, for the highest performance,

the time constants for charging and discharging must be as far apart as possible. This can be obtained by designing electrodes that exhibit high frequency dispersion, for example nano-porous metal electrodes.³² It should be noted that devices with a geometrical asymmetry but no temporal asymmetry, i.e. $\tau_{R,1} = \tau_{R,2}$ and $\tau_{L,1} = \tau_{L,2}$, produce a zero output. Thus, optimizing electrodes for high frequency dispersion is essential for the RBIP to operate.

The proposed model demonstrates that a non-linear capacitance, as observed in double layers, can result in a ratchet-like behavior. However, since the time constants in real devices vary significantly with the input signal properties, this model cannot predict the experimental performance of real devices and can only define optimal time constants for specific input signals. To fully predict and model the performance of real devices, the non-linear correlation between the input signal parameters and the charging and discharging time constants must be found. Since the frequency dispersion of the double layer capacitance is heavily affected by surface roughness, material crystallinity, and other micro-scale properties,^{31,32} such analyses must be conducted for every RBIP material and fabrication process separately and is left for future work. The model assumes that the resistance for ion transport through the pores, R_p is very high thus it accounts only for open-circuit conditions as in Figure 1i and Figure 2a-c. An equivalent circuit model that accounts for ion transport through the pores and the Ag/AgCl wires electrochemical reactions can be used to analyze other operating points. Nevertheless, as demonstrated in Figure 2g, when the Ag/AgCl wires assure that charge neutrality is maintained, the RBIP operation can be modeled as a voltage source in parallel to a resistive element which accounts for charge transport through the pores. A more thorough analysis of equivalent circuit models for the RBIP is left for future work.

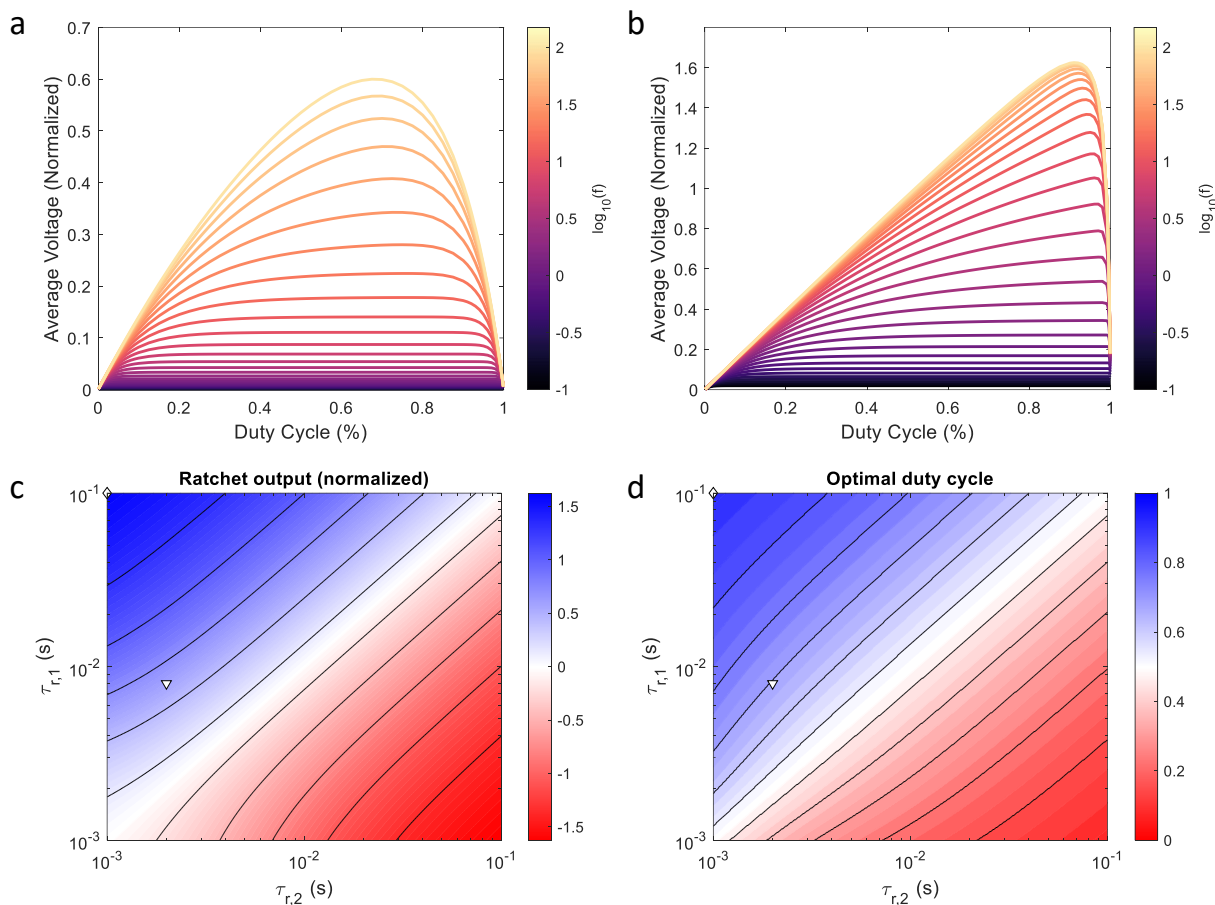


Figure 4: Device simulation | (a) The ratchet normalized output, \bar{V}_{out}/V_a , as a function of the input signal duty cycle for several input signal frequencies and $\tau_{L,2} = \tau_{R,2} = 2$ ms, $\tau_{L,1} = \tau_{R,1} = 8$ ms. (b) \bar{V}_{out}/V_a as a function of the input signal duty cycle for several input signal frequencies and $\tau_{L,2} = \tau_{R,2} = 1$ ms, $\tau_{L,1} = \tau_{R,1} = 100$ ms. (c) The RBIP normalized output \bar{V}_{out}/V_a as a function of $\tau_{R,1}$ and $\tau_{R,2}$. For each set of time constants the duty cycle is optimized to obtain the highest output (in absolute value). The frequency is 100 Hz. (d) the calculated optimal duty cycles. The triangle and the diamond mark the parameters used in a and b respectively. In all the simulations $V_a = 0.3$ V.

In conclusion, we have realized a first-of-its-kind ion pump driven by a capacitive ratchet mechanism. These ion pumps can drive a net ion flux in steady state with no redox reactions at the RBIP contacts. Ion pumping against a force was demonstrated as well as electrolyte demixing. The driving mechanism stems from the non-linear capacitance of electrode double layers, which leads to deviation in time constants between surface charging and discharging. The demonstrated ion pump can pave the way to the development of high efficiency desalination and selective ion separation systems, requiring neither moving parts nor redox reactions.

Methods

Sample preparation

RBIPs were fabricated by depositing metal contacts on both surfaces of annealed anodized aluminum oxide (AAO) wafers (InRedox Materials Innovation) with pore diameters of 20 nm, 40 nm, or 60 nm. The wafers were air annealed for ~ 10 h at temperatures of 650 °C. Several RBIP structures and recipes were tested all showing qualitatively similar results. The contacts of the sample discussed in Figures 2-3, were deposited with thermal evaporation of a chrome adhesion layer and then gold. The thickness of both layers was 40 nm (planar equivalent). The metal contacts of the sample discussed in Figure 1 were deposited with magnetron sputtering of gold (50 nm planar equivalent) followed by an 8 nm thick TiO₂ coating deposited by ALD. The ALD recipe is as described by Vega et al.³⁶ where the exposure time to the precursors was set to 1 s and the purging time was set to 5 s. The metal contacts in the samples described in Figure S2-3 were deposited with electron beam evaporation of a 10 nm thick titanium adhesion layer and then 40 nm of gold. The RBIP ion pumping properties were tested in an electrochemical cell in which the RBIP served as a membrane separating two aqueous electrolyte compartments, each containing an Ag/AgCl wire that was used to probe the voltage or current between the two compartments. In the experiments shown in Figures 2-3, parafilm was used to secure the wafers and prevent leakage. The hole diameter between each well is 0.32 cm² – this area is used for determining current density. Carbon black cloth was used to contact each conductive interface. In the experiments presented in Figures 2-3 each compartment in the electrochemical cell was filled with 1 mL of electrolyte.

RBIP performance characterization

To ensure that all the observed performance is a result of a ratcheting mechanism, as opposed to artifacts induced by unwanted electronic feedbacks, all input signals and measurements are performed in two electrode setups. In Figures 2-3 the input signal was produced with a BioLogic VSP-300 multichannel potentiostat. The voltage and current measurements were conducted with a separate channel from the same potentiostat. Voltage measurements were taken with a sampling rate of 200 μs and current measurements were taken with a sampling rate of 400 μs. All the potentiostat channels were in floating mode. The RBIP performance was characterized using the following procedures. First, V_{in} was set to 0 V for 30 s. Next, the ratchet signal was introduced for 90 s. Finally, V_{in} was set to 0 V for another 60 s. \bar{V}_{out} was calculated according to $\bar{V}_{out} = \bar{V}_{out,ON} - (\bar{V}_{out,OFF_1} - \bar{V}_{out,OFF_2})/2$ and \bar{I}_{out} was calculated according to $\bar{I}_{out} = \bar{I}_{out,ON} - (\bar{I}_{out,OFF_1} - \bar{I}_{out,OFF_2})/2$. $\bar{V}_{out,ON}$ and $\bar{I}_{out,ON}$ are respectively the voltage and current averaged over the last 30 seconds of the period in which the input signal was applied. \bar{V}_{out,OFF_1} and \bar{I}_{out,OFF_1} are respectively the voltage and current averaged over the last 15 seconds in the first (30 seconds long) period in which $V_{in} = 0$ V. \bar{V}_{out,OFF_2} and \bar{I}_{out,OFF_2} are respectively the voltage and current averaged over the last 30 seconds of the second OFF period.

In the experiment described in Figure 3, the duration of the first set of ON cycles was 5 minutes after which the ratchet was turned OFF ($V_{in} = 0$ V) for 30 s. In later sets, the ratchet ON duration was 30 minutes and the OFF duration was 90 s.

In Figure S7 and Figure S10 the input signal was generated with a HP 3245A universal source. The voltage between the Ag/AgCl wires was measured with an Agilent 34401A multimeter where both instruments shared the same ground. The voltage measurement was conducted with an integration time of 1.67 s to

reduce the output signal oscillations and obtain only the net averaged voltage. The response to every input signal was measured for 300 s after which the input was set to 0 V for 300 s. $\bar{V}_{out,ON}$, \bar{V}_{out,OFF_1} and \bar{V}_{out,OFF_2} were averaged over the last 150 s of every period.

In Figure 1 the input signal was supplied with a Keysight 33510B waveform generator and voltages were measured with Keysight 34465A multimeters. The response to every input signal was measured for 60 s after which the input was set to 0 V for 60 s.

RBIP driven demixing experiments were conducted in a setup as illustrated in Figure 3a and discussed in the experimental demonstration section. The first six OFF periods were 30 seconds long and the rest were 90 seconds long. Each voltage data point in Figure 3b-d is the temporal average of the voltage between 0.25 and 0.5 of the duration of the OFF period. In some samples input of a constant bias with higher than ± 300 mV resulted in a constant, non-negligible V_{out} . This may suggest Faradaic reactivity, which was followed by degradation in the RBIP performance for some samples. In other samples, non-zero V_{out} under a constant bias was attributed to blocked pores.

Acknowledgments

We would like to acknowledge the help of Prof. Reg Penner for allowing us to work with his group members and use their thermal evaporator for the fabrication of some of the RBIPs. AH acknowledges the support of the Boris Mints Institute. JWA was supported by the Joint Center for Artificial Photosynthesis, a DOE Energy Innovation Hub, supported through the Office of Science of the United States. Department of Energy under Award No. DE-SC0004993. SA acknowledges the support of the Gordon and Betty Moore Foundation under a Moore Inventor Fellowship (GBMF grant #5641) and The Beall Family Foundation (UCI Beall Innovation Award). GS thanks the Azrieli Foundation for financial support within the Azrieli Fellows program. This work is partially funded by the European Union (ERC, ESIP-RM, 101039804).

Author contributions

GS, JWA and SA conceptualized this work, RJK, AJH, EH, CM, DL and GS conducted the investigation, AH, SA and GS designed the methodology, RJK, AJH, EH, CM and GS conducted the formal analysis and acquired the data, visualizations were designed by EJH, AH, RJK, SA and GS, the original draft was written by SA and GS, and all authors contributed to its reviewing and editing. GS and SA supervised the project, GS, SA and FMT administered it, and acquired the funding for it.

References

1. Blaustein, M. P. Calcium transport and buffering in neurons. *Trends Neurosci.* **11**, 438–443 (1988).
2. Crofts, A. R. & Wraight, C. A. The electrochemical domain of photosynthesis. *Biochim. Biophys. Acta - Rev. Bioenerg.* **726**, 149–185 (1983).
3. Robertson, R. N. Ion transport and respiration. *Biol. Rev.* **35**, 231–264 (1960).
4. Tang, C. & Bruening, M. L. Ion separations with membranes. *J. Polym. Sci.* **58**, 2831–2856 (2020).

5. Epsztein, R., DuChanois, R. M., Ritt, C. L., Noy, A. & Elimelech, M. Towards single-species selectivity of membranes with subnanometre pores. *Nat. Nanotechnol.* **15**, 426–436 (2020).
6. Sholl, D. S. & Lively, R. P. Seven chemical separations to change the world. *Nature* **532**, 435–437 (2016).
7. Kedem, O., Lau, B. & Weiss, E. A. How to Drive a Flashing Electron Ratchet to Maximize Current. *Nano Lett.* **17**, 5848–5854 (2017).
8. Kedem, O., Lau, B. & Weiss, E. A. Mechanisms of Symmetry Breaking in a Multidimensional Flashing Particle Ratchet. *ACS Nano* **11**, 7148–7155 (2017).
9. Kedem, O., Lau, B., Ratner, M. A. & Weiss, E. A. Light-responsive organic flashing electron ratchet. *Proc. Natl. Acad. Sci.* **114**, 8698–8703 (2017).
10. Roeling, E. M. *et al.* Organic electronic ratchets doing work. *Nat. Mater.* **10**, 51–55 (2011).
11. Kedem, O., Lau, B. & Weiss, E. A. How to Drive a Flashing Electron Ratchet to Maximize Current. *Nano Lett.* **17**, 5848–5854 (2017).
12. Tarlie, M. B. & Astumian, R. D. Optimal modulation of a Brownian ratchet and enhanced sensitivity to a weak external force. *Proc. Natl. Acad. Sci.* **95**, 2039–2043 (2002).
13. Parrondo, J. M. R., Blanco, J. M., Cao, F. J. & Brito, R. Efficiency of Brownian motors. *Europhys. Lett.* **43**, 248–254 (1998).
14. Jung, P. Regular and Chaotic Transport in Asymmetric Periodic Potentials : Inertia Ratchets. 18–21 (1996).
15. Rozenbaum, V. M. High-temperature brownian motors: Deterministic and stochastic fluctuations of a periodic potential. *JETP Lett.* **88**, 342–346 (2008).
16. Lau, B., Kedem, O., Schwabacher, J., Kwasnieski, D. & Weiss, E. A. An introduction to ratchets in chemistry and biology. *Mater. Horizons* **4**, 310–318 (2017).
17. Squires, T. M. Induced-charge electrokinetics : fundamental challenges and opportunities †. **3**, 2477–2483 (2009).
18. Schwemmer, C., Fringes, S., Duerig, U., Ryu, Y. K. & Knoll, A. W. Experimental Observation of Current Reversal in a Rocking Brownian Motor. *Phys. Rev. Lett.* **121**, 104102 (2018).
19. Nicollier, P. *et al.* Nanometer-Scale-Resolution Multichannel Separation of Spherical Particles in a Rocking Ratchet with Increasing Barrier Heights. *Phys. Rev. Appl.* **15**, 034006 (2021).
20. Skaug, M. J., Schwemmer, C., Fringes, S., Rawlings, C. D. & Knoll, A. W. Nanofluidic rocking Brownian motors. *Science (80-.)*. **359**, 1505–1508 (2018).
21. Liu, Z., Gu, X., Hwu, J., Sassolini, S. & Olynick, D. L. Low-temperature plasma etching of high aspect-ratio densely packed 15 to sub-10nm silicon features derived from PS-PDMS block copolymer patterns.
22. Słapik, A., Łuczka, J., Hänggi, P. & Spiechowicz, J. Tunable Mass Separation via Negative Mobility. *Physical Review Letters* **122**, (2019).
23. Motz, T., Schmid, G., Hänggi, P., Reguera, D. & Rubí, J. M. Optimizing the performance of the

- entropic splitter for particle separation. *J. Chem. Phys.* **141**, 074104 (2014).
24. Reguera, D. *et al.* Entropic splitter for particle separation. *Phys. Rev. Lett.* **108**, 1–5 (2012).
 25. Yang, B., Long, F. & Mei, D. C. Negative mobility and multiple current reversals induced by colored thermal fluctuation in an asymmetric periodic potential. *Eur. Phys. J. B* **85**, 2–7 (2012).
 26. Siwy, Z. & Fuliński, A. A nanodevice for rectification and pumping ions. *Am. J. Phys.* **72**, 567–574 (2004).
 27. Siwy, Z. & Fuliński, A. Fabrication of a Synthetic Nanopore Ion Pump. *Phys. Rev. Lett.* **89**, 4–7 (2002).
 28. Wu, X., Ramiah Rajasekaran, P. & Martin, C. R. An Alternating Current Electroosmotic Pump Based on Conical Nanopore Membranes. *ACS Nano* **10**, 4637–4643 (2016).
 29. Herman, A., Ager, J. W., Ardo, S. & Segev, G. Ratchet-Based Ion Pumps for Selective Ion Separations. *PRX Energy* **2**, 023001 (2023).
 30. Bazant, M. Z., Thornton, K. & Ajdari, A. Diffuse-charge dynamics in electrochemical systems. *Phys. Rev. E* **70**, 021506 (2004).
 31. Kerner, Z. & Pajkossy, T. On the origin of capacitance dispersion of rough electrodes. *Electrochim. Acta* **46**, 207–211 (2000).
 32. Pajkossy, T. Impedance spectroscopy at interfaces of metals and aqueous solutions — Surface roughness, CPE and related issues. *Solid State Ionics* **176**, 1997–2003 (2005).
 33. Rozenbaum, V. M., Shapochkina, I. V., Teranishi, Y. & Trakhtenberg, L. I. Symmetry of deterministic ratchets. *Phys. Rev. E* **100**, 22115 (2019).
 34. Bazant, M. Z., Kilic, M. S., Storey, B. D. & Ajdari, A. Towards an understanding of induced-charge electrokinetics at large applied voltages in concentrated solutions. *Adv. Colloid Interface Sci.* **152**, 48–88 (2009).
 35. Galama, A. H., Post, J. W., Hamelers, H. V. M., Nikonenko, V. V. & Biesheuvel, P. M. On the origin of the membrane potential arising across densely charged ion exchange membranes: How well does the teorell-meyer-sievers theory work? *J. Membr. Sci. Res.* **2**, 128–140 (2016).
 36. Vega, V. *et al.* Diffusive transport through surface functionalized nanoporous alumina membranes by atomic layer deposition of metal oxides. *J. Ind. Eng. Chem.* **52**, 66–72 (2017).

Supporting information for A nanoporous capacitive electrochemical ratchet for continuous ion separations

Rylan J. Kautz¹, Alon Herman², Ethan J. Heffernan¹, Camila Muñetón^{3,4}, David Larson^{5,6}, Joel W. Ager III^{5,6,7,8}, Francesca M. Toma^{5,6} Shane Ardo^{1,3,9*} and Gideon Segev^{2,5,6**}

¹Department of Materials Science & Engineering, University of California, Irvine, CA 92697, USA

²School of Electrical Engineering, Tel Aviv University, Tel Aviv 6997801, Israel

³Department of Chemistry, University of California, Irvine, CA 92697, USA

⁴Department of Chemistry, University of Massachusetts, Boston, MA 02125 USA⁷

⁵Chemical Sciences Division, Lawrence Berkeley National Lab, Berkeley, CA 94720, USA

⁶Joint Center for Artificial Photosynthesis, Lawrence Berkeley National Lab, Berkeley, CA 94720, USA

⁷Materials Sciences Division, Lawrence Berkeley National Lab, Berkeley, CA 94720, USA

⁸Department of Materials Science and Engineering, University of California Berkeley, CA 94720, USA

⁹Department of Chemical & Biomolecular Engineering, University of California, Irvine, CA 92697, USA

*Email: ardo@uci.edu

**Email: gideons1@tauex.tau.ac.il

Sample setup

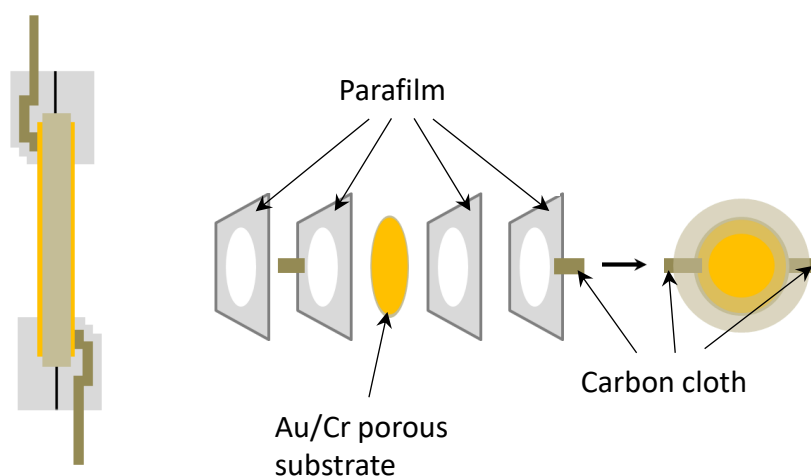


Figure S1: A schematic illustration of an RBIP sample

Time constants extraction- frequency sweep

The sample analyzed in Figure 1g,h was also measured at various input signal frequencies. The duty cycle is 0.5, and the amplitude is $V_a=0.7$ V. The electrolyte is 0.2 mM NaCl aqueous solution. All other parameters are as described in figure 1. Figure S2(a-c) show respectively the average temporal responses of V_L , V_R and V_{out} . For clarity, the time for every signal was normalized by its period. The input signal frequency f is indicated by the colorbar. For the lowest frequency (0.1 Hz) three temporal periods were averaged to obtain the average response, for a frequency of 0.2 Hz, 8 periods were averaged, and for higher frequencies at least 15 periods were averaged. The solid lines show the best exponential fit to the measured data. Figure S3a shows the extracted time constants for the two parts of the input signal ($0 < t < d_c T$, and $d_c T < t < T$) and each of the measured signals. The time constants for all signals drop significantly with the input signal frequency demonstrating the frequency dispersion. Differences between the time constants for the two parts of the input signals are also observed. Figure S3a shows the extracted time constants and Figure S3b shows the extracted values of V_f for each of the signals. Because the effective time constants increase as the frequency decreases, V_f saturates at the applied voltage only for very low frequencies. As a result, the amplitude of the effective signal applied to the ratchet also decreases with frequency.

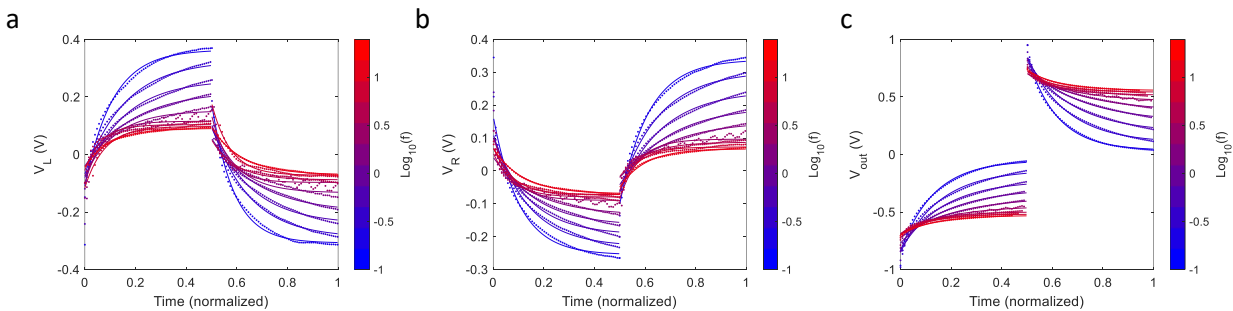


Figure S2: (a-c) The averaged responses of $V_L(t)$, $V_R(t)$ and $V_{out}(t)$ respectively for various input signal frequencies. The sample is as in Figure 1. The duty cycle is 0.5, and the amplitude is $V_a=0.7$ V. The electrolyte is 0.2 mM NaCl aqueous solution. For each signal, the time was normalized by input signal temporal period. The color bar indicates the input signal frequency. The symbols mark the measured signals, and the solid lines are the exponential fit. The plotted measured signals were under sampled for visualization purposes.

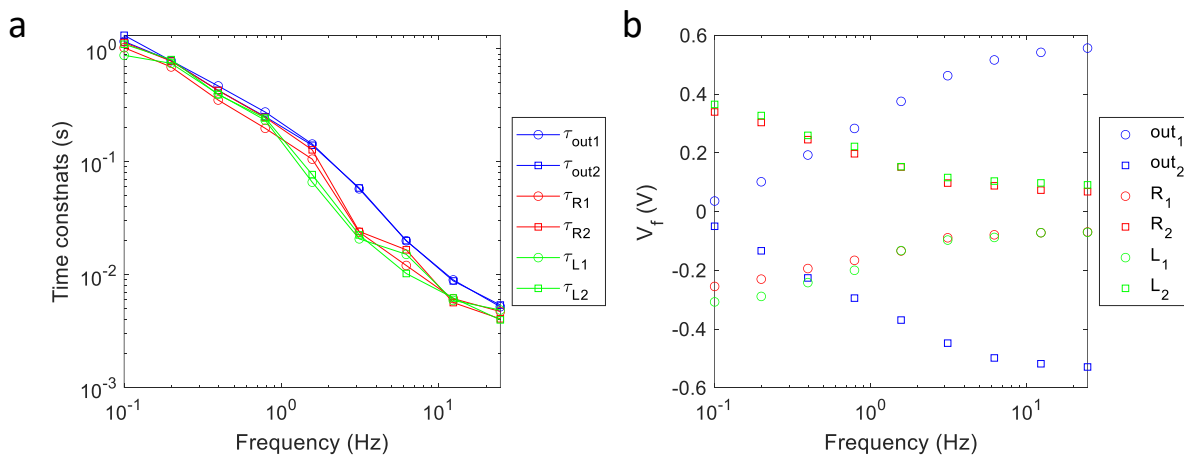


Figure S3: the extracted time constants (a) and V_f (b) for the signals shown in Figure S2.

The average responses for the data presented in Figure 2

Figure S4 a-e shows the measured average response $V_{out}(t)$ for various duty cycles and frequencies of 1, 5, 10, 25, 50, 125 Hz in (a-e) respectively. Each output is the averaged response of at least 30 temporal periods.

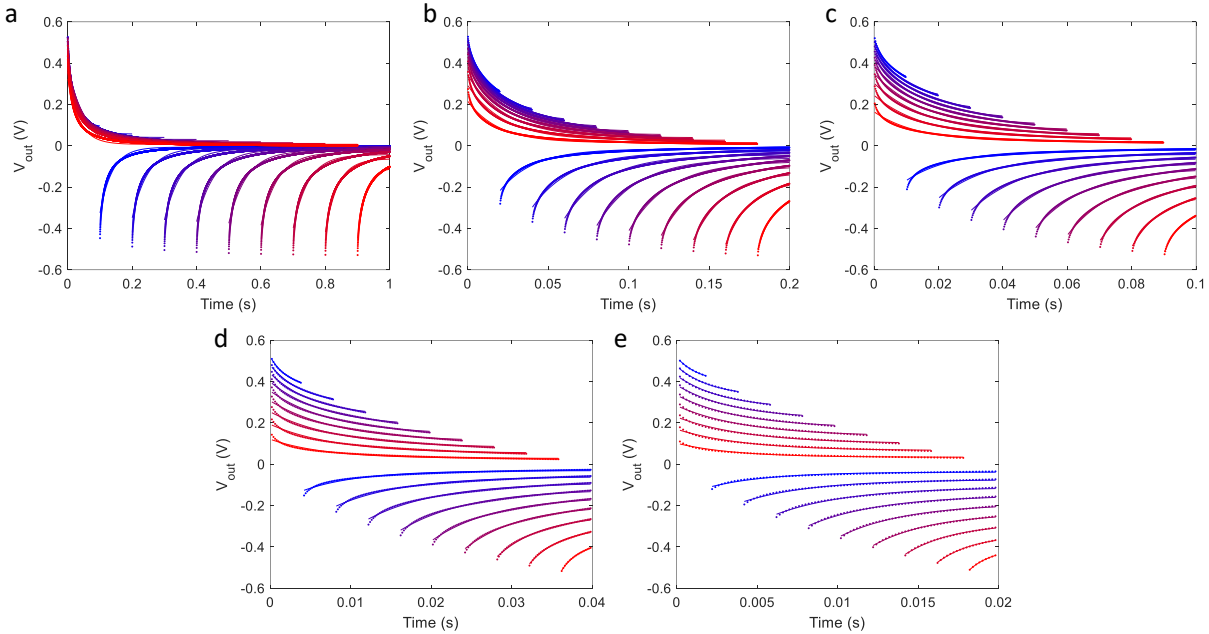


Figure S4: Measured $V_{out}(t)$ for various duty cycles (dots) and the best fit to single exponential functions. The color coding matches the input signal duty cycle. The input signal frequencies are 1, 5, 10, 25, 50, 125 Hz in (a-e) respectively. Each output is the averaged response of at least 30 temporal periods.

Figure S5a shows the average temporal response of $I_{out}(t)$. The RBIP and signal parameters are as in Figure 2a. The measured current is normalized by the RBIP active area ($A = 0.32 \text{ cm}^2$), and the time is normalized by the temporal period of every signal. The response for other duty cycles and the best fit to exponential functions are shown in supporting figure S6. Figure S5b shows the time constants obtained from $I_{out}(t)$. As in the time constants obtained from the voltage measurement, the current time constants vary significantly with frequency and duty cycle, and the time constants of the first part of every period are close to those of the second part of the period flipped with respect to a duty cycle of 0.5. The color coding is as in Figure S5a.

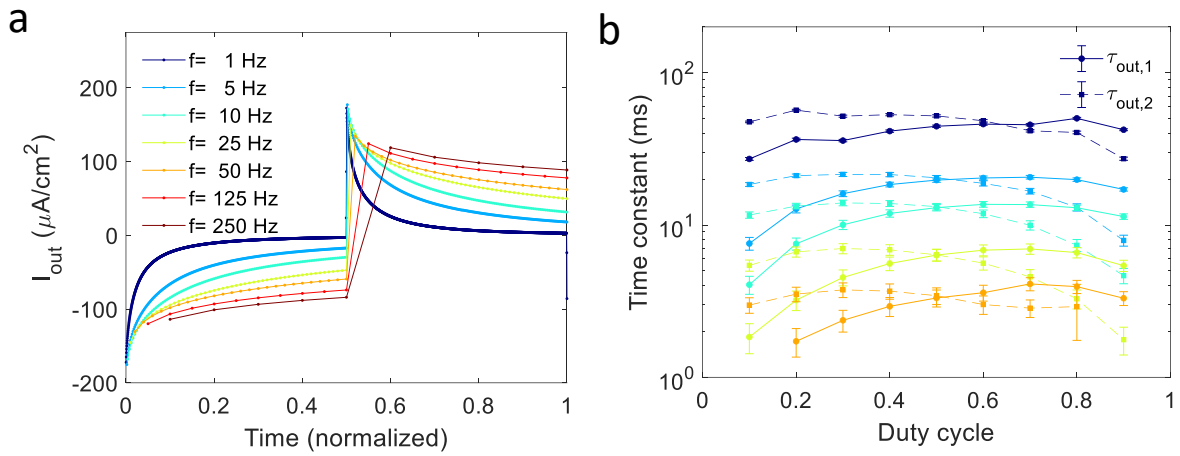


Figure S5: (a) The current density, I_{out}/A , as a function of time for several input signal frequencies and a duty cycle of 0.5. (b) the time constants of I_{out} for several input signal frequencies and duty cycles. The solution is 1 mM HCl aqueous solution, the RBIP pore diameter is 40 nm, the active area of the membrane is $A = 0.32 \text{ cm}^2$, and the input signal amplitude, V_{in} , is 0.3 V.

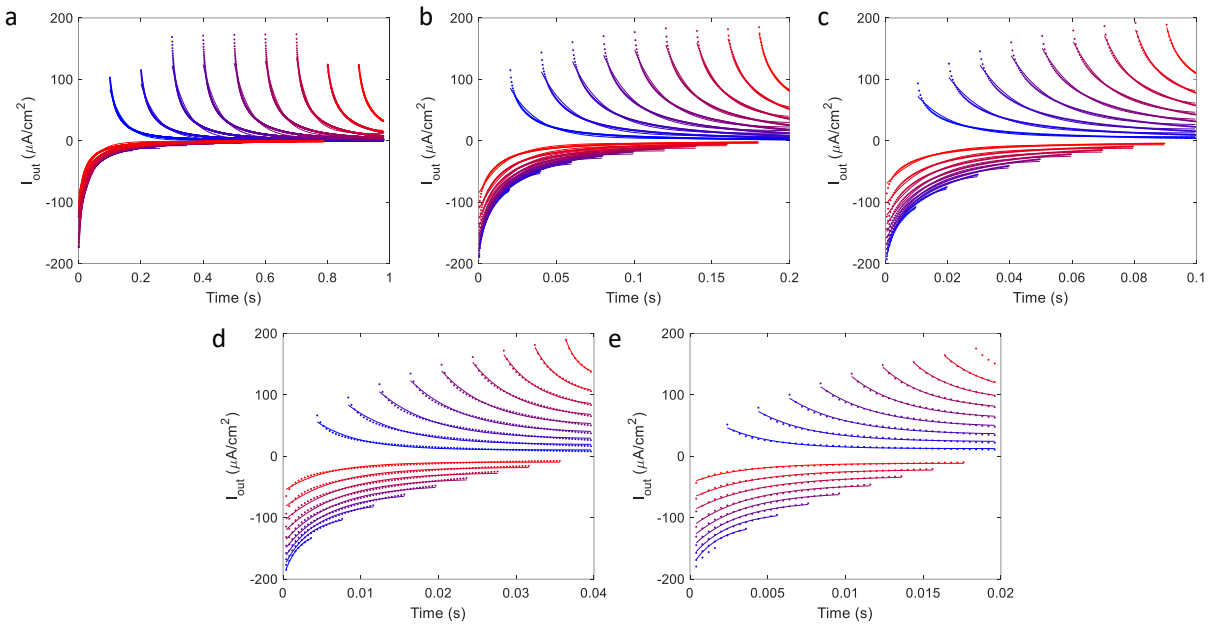


Figure S6: Measured $I_{out}(t)$ for various duty cycles (dots) and the best fit to single exponential functions. The color coding matches the input signal duty cycle. The input signal frequencies are 1, 5, 10, 25, 50, 125 Hz in (a-e) respectively. Each output is the averaged response of at least 30 temporal periods.

Other results and methods

RBIP with a pore diameter of 40 nm in KCl aqueous electrolyte

Here we have tested the performance of an RBIP fabricated on AAO wafers with 40 nm diameter pores. The wafers were air annealed for 11 hours at 650 °C. The contacts were deposited with electron beam evaporation of 10 nm of titanium and 40 nm of gold (planar equivalent). For the results presented in this section, unless stated otherwise, the input electric signal $V_{in}(t)$ is a rectangular wave at a frequency of 100 Hz, and the amplitude V_a is 0.2 V. The ratchet input signal, V_{in} , was applied with HP 3245A universal source and the voltage between the Ag/AgCl wires was measured with Agilent 34401A multimeter, where both instruments shared the same ground. The voltage measurement was conducted with an integration time of 1.67 seconds to reduce the output signal oscillations and obtain only the net time averaged voltage, \bar{V}_{out} . The response to every input signal was measured for 5 min after which the input was set to 0 V for 5 min. Figure S7a shows the recorded voltage for duty cycles between 5% and 100% (the duty cycle is the portion of the time in every period where the voltage is at its high value. The input signal duty cycle is marked next to the output curve in Figure S7a).

Once a ratchet signal commences, \bar{V}_{out} quickly builds up to a level determined by the duty cycle. The ratchet induced voltage reaches its largest values for duty cycles close to 50%, i.e., a temporally averaged input voltage of 0 V. For a duty cycle of 100%, which is the response to a voltage step from 0 V to 0.2 V, the voltage signal shows the well expected, fast capacitive charging behavior corresponding to polarization of the metal contacts. However, unlike the response to a duty cycle of 100%, for a duty cycle of 95% (a temporal average input voltage of 0.19 V), a ratchet action is observed and the response has a negative sign with a much slower decay time. This provides a simple distinction between steady-state ratchet-powered transport and capacitive charging–discharging behavior.

To estimate the ratchet output voltage, the voltage was averaged over the last 2.5 min of every cycle and the difference between the ratchet ON and ratchet OFF average voltages was calculated. Figure S7b shows the ratchet time averaged output voltage, \bar{V}_{out} , as a function of the input signal amplitude, V_a , for 1 mM and 10 mM KCl aqueous solutions. More details on how \bar{V}_{out} is calculated can be found in the methods section. The input signal was a square wave with a voltage offset of 0 V, frequency of 100 Hz and a duty cycle of 50%. For the 1 mM KCl solution, a noticeable ratchet output is visible for ratchet signals with an amplitude as small as 0.05 V. This extremely low voltage threshold provides a clear distinction between ratchet induced ion transport, where the voltage threshold is about $2kT$ (k is the Boltzmann constant and T is the temperature (K)), and ion transport induced by chemical reactions where the threshold bias is determined by the Gibbs free energy and the reaction overpotentials. The ratchet output is significantly smaller in the 10 mM KCl solution. This is an expected result, because at a higher ion concentration potential screening is more significant, and as a result the center of the pore is less affected by the input signal and serves as a shunt. Figure S7c-d show the ratchet output voltage as a function of the frequency and duty cycle in 1 mM and 10 mM KCl, respectively. Since ratchet systems have no output when a DC voltage is applied, the RBIP output voltage is close to 0 V for duty cycles near 0 % and 100 %. Similarly, at low frequencies, the RBIP fully charges and discharges the double layers, which is similar to operation under DC bias. Thus, the output is near 0 V at low frequencies as well. As a result, the RBIP shows a significant output only when operated with duty cycles near 50% and at input signal periods that are close to the characteristic charging–discharging time constant of the RBIP. When the input signal period is significantly shorter than the RBIP charging and discharging time constants the output goes to zero again.

The output of the ratchet was measured when switching the leads of the ratchet, and the leads of the Ag/AgCl voltage measurements. Figure S8a shows the measurement setup and Figure S8b shows \bar{V}_{out} as a function of the duty cycle for every measurement configuration. Switching the positive and negative leads for V_{in} (Ratchet switch in Figure S8a-b) resulted in \bar{V}_{out} values that were reflected around 50% duty cycle such that $\bar{V}_{out,1}(\text{duty cycle}) = \bar{V}_{out,2}(1 - \text{duty cycle})$; switching the positive and negative leads for \bar{V}_{out} (Ag/AgCl switch in Figure S8a) resulted in oppositely-signed values for \bar{V}_{out} such that $\bar{V}_{out,1}(\text{duty cycle}) = -\bar{V}_{out,2}(\text{duty cycle})$.

Water pumping through the RBIP was not noticed in any of the experiments that were conducted.

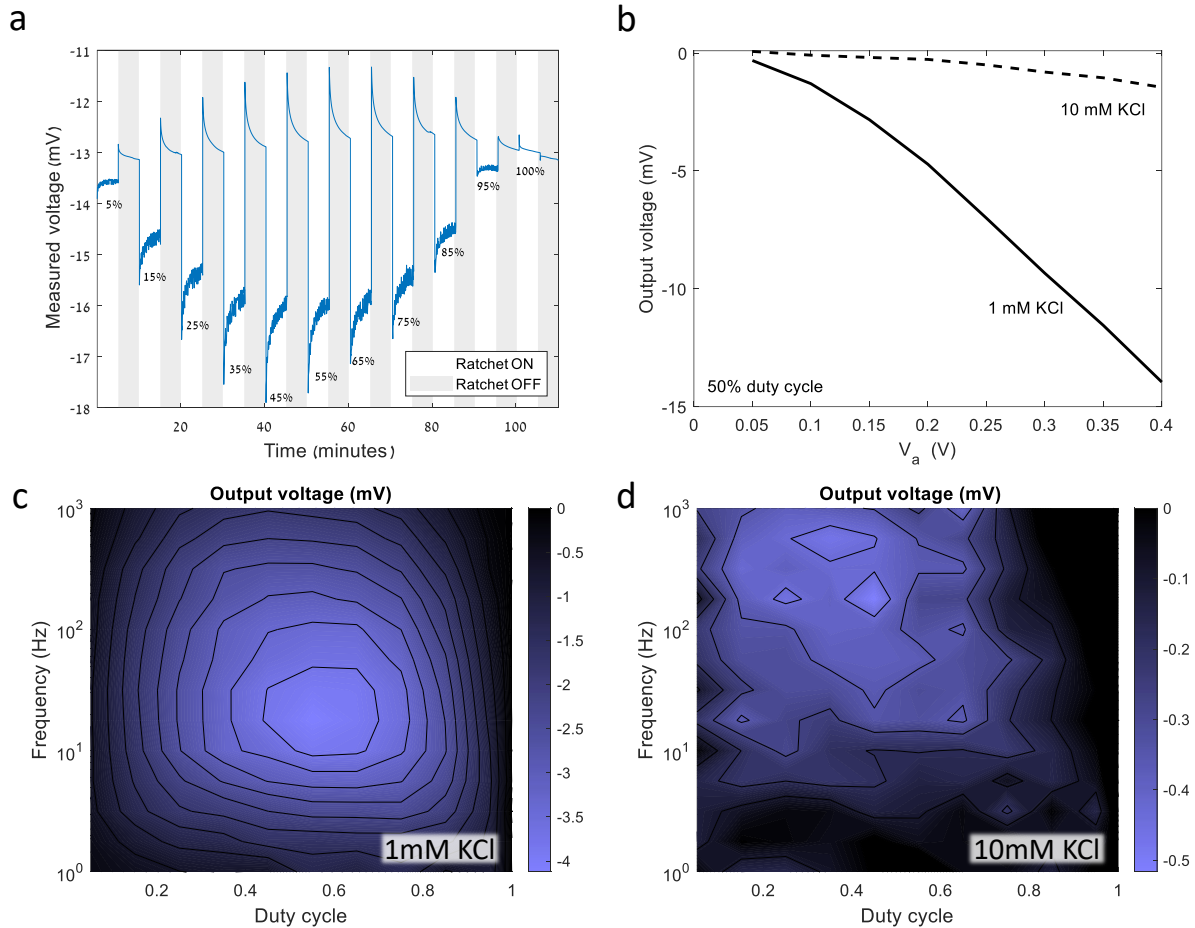


Figure S7: The output of a RBIP sample with 40 nm pores. (a) Measured output voltage, \bar{V}_{out} , for an input signal with various duty cycles. The input signal is a rectangular wave with V_a of 0.2 V, a frequency of 100 Hz, and the electrolyte is 1 mM KCl. (b) The ratchet output voltage as a function of the input signal amplitude, the frequency is 100 Hz, and the duty cycle is 50%. (c,d) the ratchet output voltage as a function of the input signal frequency and duty cycle. The input signal is a rectangular wave with V_a of 0.2 V. The electrolyte is 1 mM KCl (c), and 10 mM KCl (d).

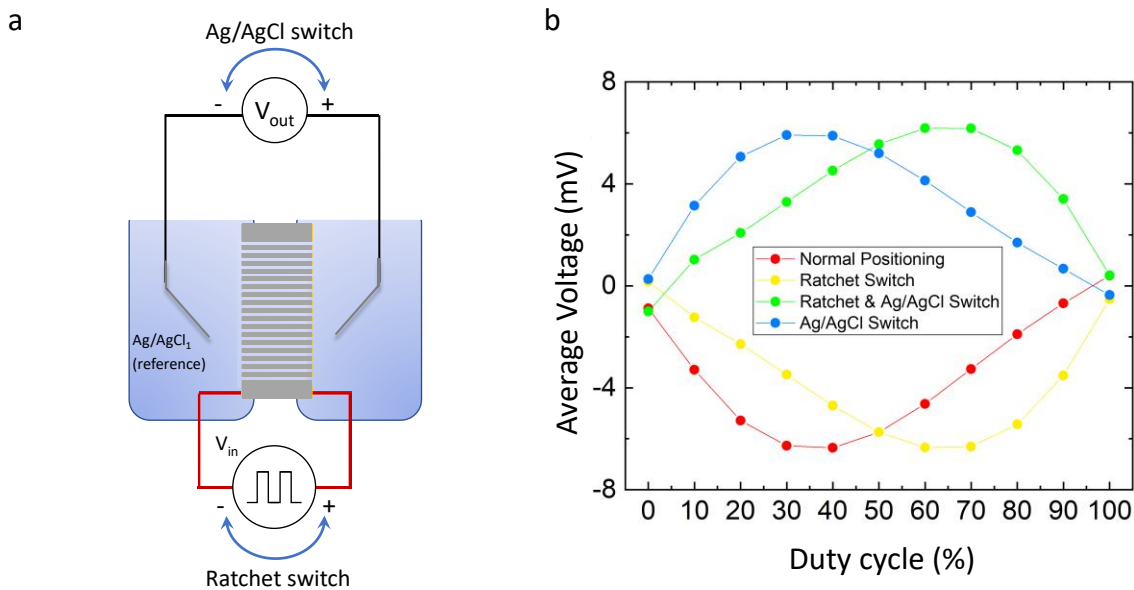


Figure S8: (a) an illustration of the lead switching experiment, (b) The voltage output of an RBIP when switching the input signal leads, and the leads of the Ag/AgCl voltage measurements. The input signal frequency is 50 Hz and the solution is 1 mM HCl. All the rest RBIP and input signal parameters are in as in Fig 2,

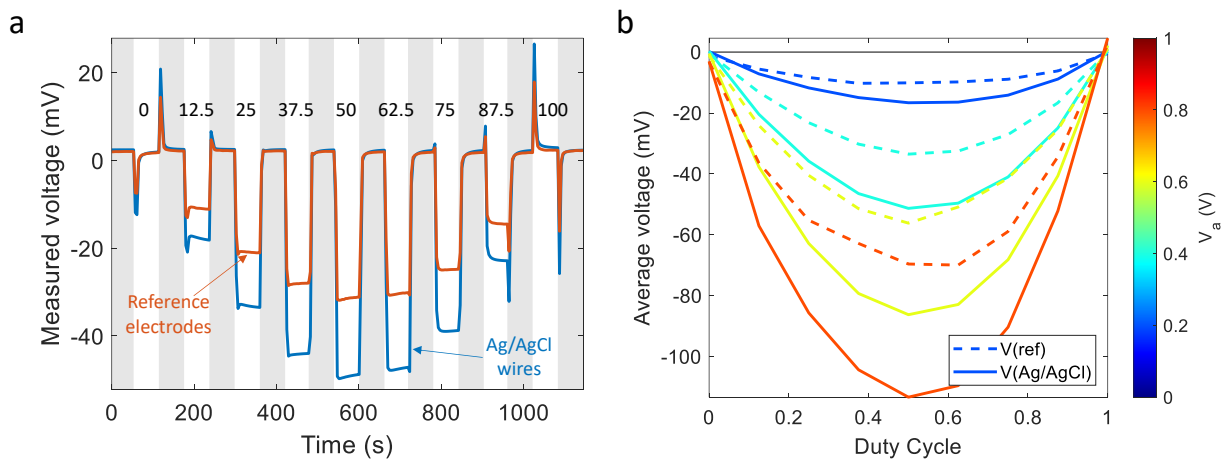


Figure S9: (a) the voltage output measured between two Ag/AgCl wires and two leak-free reference electrodes. The pore diameter is 40 nm, the electrolyte is 0.2 mM KCl aqueous solution, the signal frequency is 100 Hz, and the amplitude is $V_a = 0.4$ V. The time periods in which the ratchet operated are the bright areas and the shaded areas are time periods in which the input voltage was set to 0 V. The duty cycle (in percent) used is noted next to the curves. (b) The average ratchet voltage, \bar{V}_{out} , as a function of the duty cycle and several input signal amplitudes measured between two leak-free reference electrodes (dashed line) and Ag/AgCl wires (solid line).

RBIP with a pore diameter of 20 nm operation in KCl aqueous electrolyte

The same set of measurements was repeated using a RBIP constructed on an AAO wafer with 20 nm diameter pores. The sample was air annealed for 11 hours at 650 °C and the contacts were deposited by electron beam evaporation of 30 nm of titanium and 20 nm of gold (planar equivalent). Figure S10a shows typical data for the measured ratchet signal for an input signal frequency of 100 Hz and duty cycles between 5 and 95%. The solution is 1 mM KCl. The input signal parameters are as in Figure S7a. As discussed above, the ratchet signal was turned ON for 5 min and then the voltage was set to 0 V for 5 min. Unlike the 40 nm pore sample, the response to the ratchet signal does not go to 0 V for duty cycles near 0 and 1. This can be attributed to partial blocking of the pores, caused by their smaller diameter. Further discussion of the effect of blocked pores and other failure modes in RBIP devices can be found in the failure modes section.

Figure S10b shows the 20 nm pore RBIP output \bar{V}_{out} , as a function of the input signal amplitude V_a in 1 mM KCl and 10 mM KCl aqueous solutions. The ratchet output is defined as in Figure S7. The frequency is 100 Hz and the duty cycle is 50 %. A noticeable output was recorded for amplitudes as low as 50 mV demonstrating an extremely low voltage threshold. When compared to the 40 nm pore RBIP, the performance of the 20 nm pores RBIP is significantly higher at the higher ionic strength solution. Since in these samples the pore diameter is closer to the Debye length, the electric potential modulation affects a larger portion of the pore. As a result, the decrease in performance with the ionic strength is less pronounced in these RBIPs. Figure S10c-d shows \bar{V}_{out} as a function of the input signal duty cycle and frequency for 1 mM KCl and 10 mM KCl aqueous solutions, respectively. In 1 mM KCl aqueous solution, the RBIP optimal ratchet frequency and duty cycle are 56 Hz and 0.25 respectively which yield an output of -7.5 mV. In 10 mM KCl solution, the optimal frequency and duty cycle are 316 Hz and 0.35 respectively and the output is -1.9 mV. The optimal operating frequency increases with the ionic strength and the 20 nm pores RBIP outperforms the 40 nm pores RBIP in higher concentration solutions.

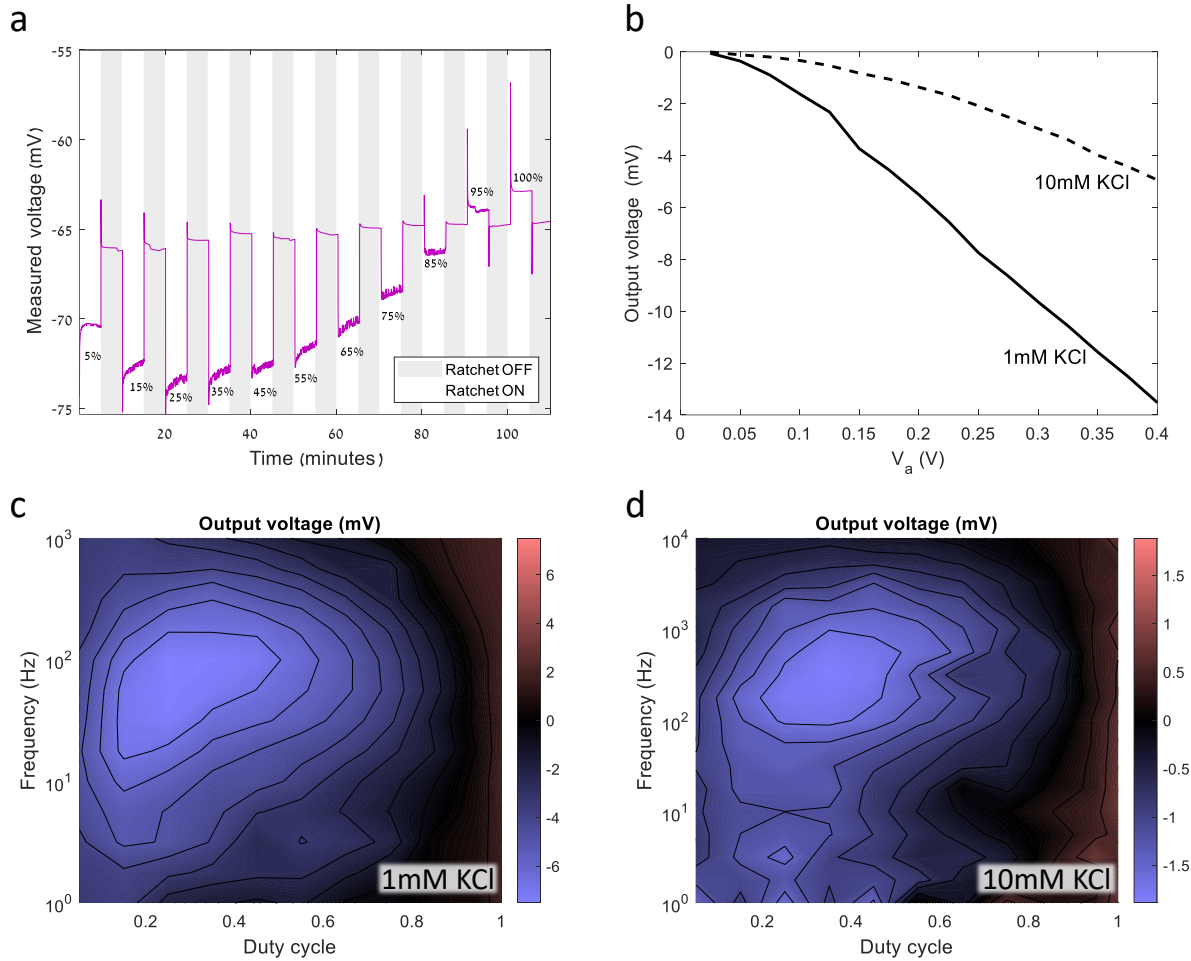


Figure S10: The output of RBIPs with 20 nm pores. (a) The measured voltage for input signals with various duty cycles. The input signal is a square wave with V_a of 0.2 V, the frequency is 100 Hz and the electrolyte is 1 mM KCl. (b) The ratchet output voltage as a function of the input signal amplitude, V_a , the frequency is 100 Hz and the duty cycle is 50%. (c,d) the ratchet output voltage as a function of the input signal frequency and duty cycle. The input signal is a square wave with V_a of 0.2 V. The electrolyte is 1mM KCl (c) and 10mM KCl (d).

Ratchet driven demixing

Figure S11a,b shows respectively \bar{V}_{out} (a) and \bar{I}_{out} (b) as a function of duty cycle for the sample used for the demixing experiment.

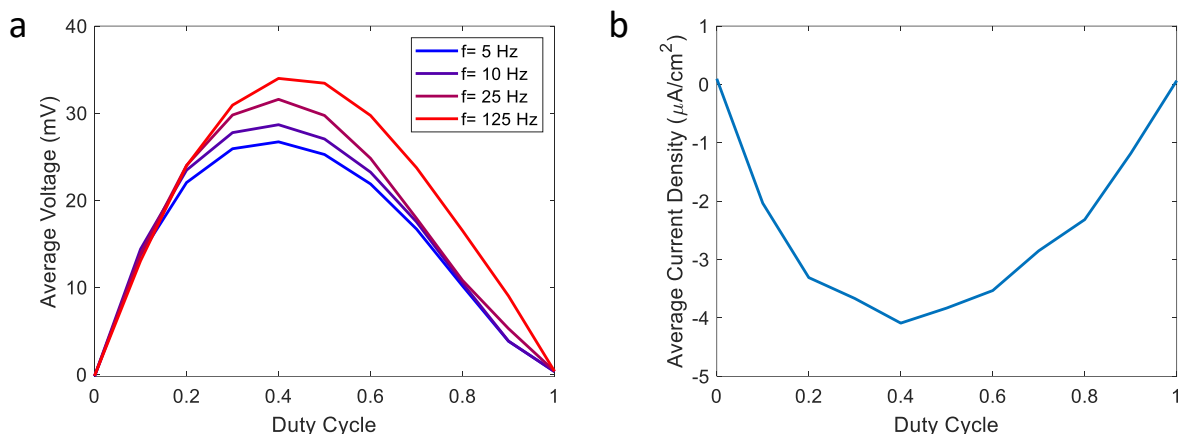


Figure S11: \bar{V}_{out} (a) and \bar{I}_{out} (b) as a function of duty cycle for the sample used for the demixing experiment discussed in Figure 3. This input signal amplitude is $V_a = 0.3$ V, for (b) the input signal frequency is 125 Hz. The solution in (a,b) is 1 mM HCl aqueous solution.

Figure S12(a-c) shows the demixing measurements discussed in Figure 3b focusing on specific cycles of ratchet ON-OFF periods. The red curves (right vertical axis) show the time averaged current measured between the Ag/AgCl meshes. Every data point is obtained by averaging the current over 1 s. The current response can be described in terms of two transient components. The first component is a faster current decline (in absolute value) which decays after 5 minutes. This is the response for pumping ions that back-diffused while the ratchet was turned OFF during voltage measurements. After this initial response, the current declines much more gradually. This slow decline may be a result of the build-up of a cation concentration gradient as described above. This assumption is supported by measured voltage which saturates in a similar manner.

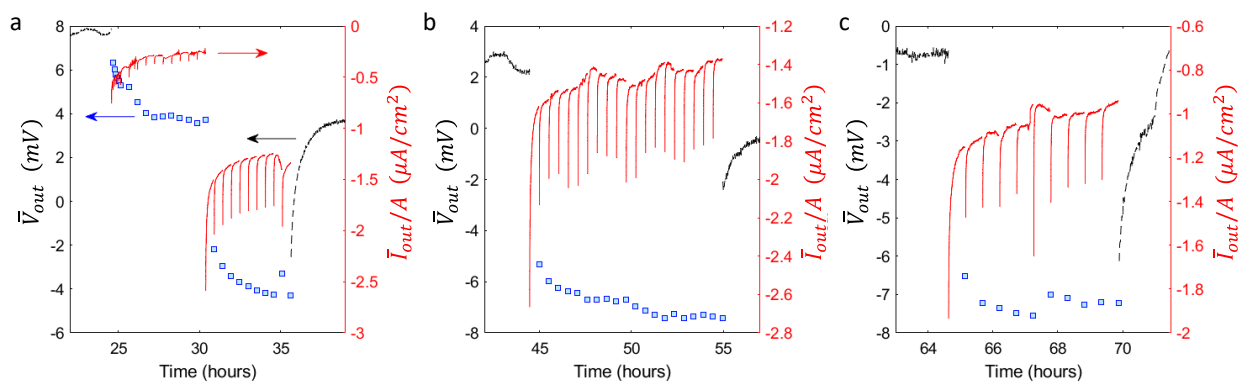


Figure S12. Same measurements as in Figure 3(b) focusing on specific times. The red curves are the average currents measured between the Ag/AgCl meshes normalized by the RBIP area. The input signal is a rectangular wave with duty cycle of 0.5, frequency of 125 Hz an

Comparison to electronic flashing ratchets

The RBIP described here is similar in function to flashing ratchets in the sense that particle transport is driven by internal potential fluctuations^{1,2} and not by a voltage that is applied to external electrodes (as in rectifying ionic diodes^{3,4} and rocking ratchets^{1,2}). Thus, it is interesting to compare the obtained outputs to those reported in previous demonstration of flashing ratchets. The ratio of the ratchet input signal amplitude, V_a , to the magnitude of the steady-state output voltage, \bar{V}_{out} or current, \bar{I}_{out} , are key parameters used to quantify the efficiency of a ratcheting process. In many of the previous demonstrations of flashing ratchets (which are closest in function to the RBIP reported here),⁵⁻⁸ which all used electronic charge carriers, V_a is applied to electronic conductors that are isolated from charge transport layer to avoid shunts. Since there is a significant electric potential drop across the isolation layers, a large amplitude is required. In the RBIP architecture the input signal, V_a , is applied to the metal contacts that are deposited on top of the AAO membrane and charge transport across the metal|solution interface is possible only by inducing redox reactions. Thus, there will be no charge transport across this interface, if no exogenous species are added and/or the amplitude of V_a is kept small. As a result, there is no need to isolate the contacts between the ratchet and the media in which the output charge transport takes place, and thus lower input signals can be applied. In the RBIP discussed in Figure 1 a TiO₂ ALD layer is deposited on top of the contacts to protect it from degradation and to assure that no redox reactions take place at the contacts. Nevertheless, as demonstrated with the other RBIPs tested, the RBIP can drive ion transport with no associated redox reactions without this layer (Figure 2-3, and the section “*Other results and methods*” in the supporting information).

Calibration of V_{out} response from aqueous HCl concentration ratios across an RBIP

The correlation between the HCl concentration difference and the Ag/AgCl voltage was obtained by measuring the voltage between two Ag/AgCl wires placed in the cell filled with two solutions with predefined concentrations. Figure S13 shows the measured voltage as a function of the concentration ratio between the cells. However, it should be noted that variability between samples, and changes in the pore surface charge due to the long exposure to acidic conditions may lead to an inaccuracy in the concentration difference estimation.

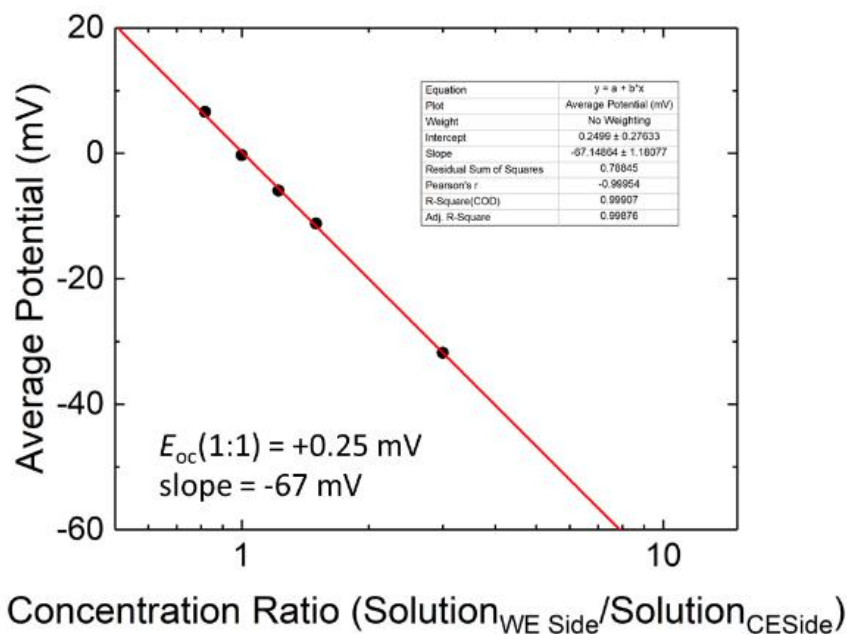


Figure S13: The measured Ag/AgCl voltage when a concentration gradient was intentionally introduced between the two compartments. The input signal is $V_{in} = 0$ V, the reference concentration is 1 mM HCl.

Sample degradation

As prepared samples have shown a pumping performance that is significantly higher than presented in Figure S7. However, this higher performance degraded in the first several hours of operation. Figure S14a shows the recorded output of the RBIP discussed in Figure S7 during its first 20 hours of its operation. In this measurement, the as-prepared RBIP is operated with an input signal as described in Figure S7b with an amplitude of 0.4V repeatedly until its performance stabilized. Only once the performance has stabilized the measurements presented in Figure S7a-d where conducted. In many of the tested samples post-mortem analysis revealed no noticeable changes in morphology. In such cases, failure may be a result of changes in the surface charge distribution within the pore leading to a change in the electric potential distribution within the RBIP. In other samples structural changes were visible. Figure S14b shows an EDS map overlaid on top of an SEM image of an as-prepared RBIP in which the contacts were deposited with electron beam evaporation. As shown in Figure S14b, the as prepared samples have a uniform coverage of gold which allows effective biasing of the pores. Samples prepared with other methods had a similar structure. Figure S14c-d shows respectively an SEM image and an EDS map overlaid on top of the SEM image of an RBIP that was operated for about 24 hours. As can be seen in Figure S14c-d, clustering of gold forms islands that block some of the pores but also prevents effective biasing of the pores that are not

blocked thus leading to a significant reduction in the pumping performance. In other samples, failure was a result of contact delamination.

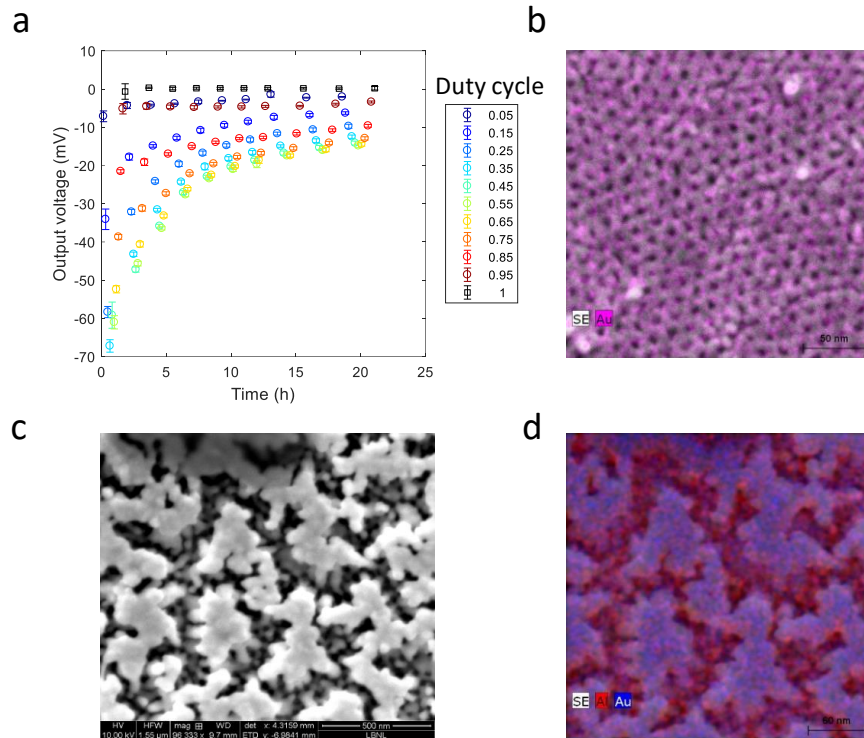


Figure S14: Stability analysis of an RBIP. (a) the ratchet output of an as-deposited sample cycled between different duty cycles for 21 hours. (b) SEM and EDS overlay of an as-deposited sample with 20 nm pores. (c) An SEM image of a sample after 25 hours of operation.

Failure modes

The trivial failure modes that can affect the RBIP performance are the shunting and blocking of pores. Understanding the effect of these failure modes can help shed light on the contributions to the performance of different devices. When entire pores, or parts of the pores are shunted, the electric potential distribution within the shunted regions is unaffected by the ratchet signal. As a result, the shunted regions provide a path for ions to diffuse back toward their equilibrium distribution thus limiting the RBIP pumping performance. When the salinity level is too high such that the Debye length is significantly smaller than the pore radius, the center of the pore will not be perturbed by the ratchet signal thus forming a shunt. Another cause for pore shunting is improper biasing of the pore, for example when the metal layer does not cover the entire surface of the AAO wafer.

When pores are blocked, or when the resistance to transport through them is too high, the device can be effectively described as two separate compartments where the voltage difference between the two compartments is determined by the ratchet signal. In such case, the time averaged voltage output, \bar{V}_{out} is simply the average voltage applied to the RBIP thus it is linear with the duty cycle. Furthermore, if the pores are almost entirely blocked, the output is less affected by changes in the solution conductivity. Figure S15a-b shows an example of the output of an RBIP with blocked pores. The RBIP pore diameter is 20 nm and the deposited metal layers are 40 nm of titanium and 40 nm of gold. Figure S15a shows the measured V_{out} for an input signal with V_a of 0.2 V, a frequency of 100 Hz and duty cycles between 5% and 95%. All the measurement parameters are as in Figure S7a. The solution is 1 mM KCl and 10 mM KCl.

Figure S15b shows the computed \bar{V}_{out} as a function of the input signal duty cycle. The linear relation between the output and the duty cycle, and the small change of output with the salinity indicates that transport through the pores is too resistive or that the pores are blocked. Similarly, when an alumina membrane was used that did not intentionally have pores in it, \bar{V}_{out} values were largest for 0% and 100% duty cycle, and zero for 50% duty cycle, further supporting a ratchet-based mechanism for our RBIPs.

Clearly, some devices may have regions that operate well, regions that are fully or partially shunted and other regions that are fully or partially blocked. In such case, the measured signal will be a convolution of the ratchet output, which is zero at duty cycles of 0 and 100% but is nonzero elsewhere, the contribution of shunted regions, which is zero for all duty cycles, and the contribution of highly resistive, or blocked regions that is linear with the duty cycle. Thus, partially blocked areas, or high resistance for ion transport within the pore, may be the reason for the non-zero \bar{V}_{out} obtained in RBIPs with pore diameter of 20 nm. Figure S16 shows another example for \bar{V}_{out} as a function of the duty cycle for an RBIP where the pores are partially blocked. The sample and input signal parameters are as in Figure 2 and the solution is 1mM HCl. The output curve is superimposed on a linear trend which is indicative of partial blockage of the pores.

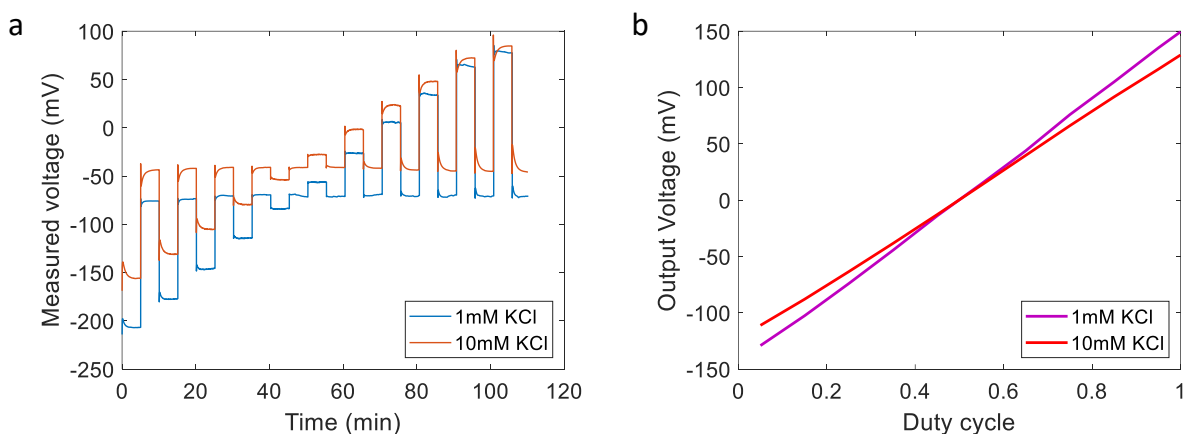


Figure S15: the ratchet output for an RBIP with partially blocked 20 nm pores (a) The measured output voltage for an input signal with various duty cycles. The input signal is a square wave with V_o of 0.2 V, the frequency is 100 Hz. (b) the time averaged output voltage, \bar{V}_{out} , as a function of the input signal duty cycle.

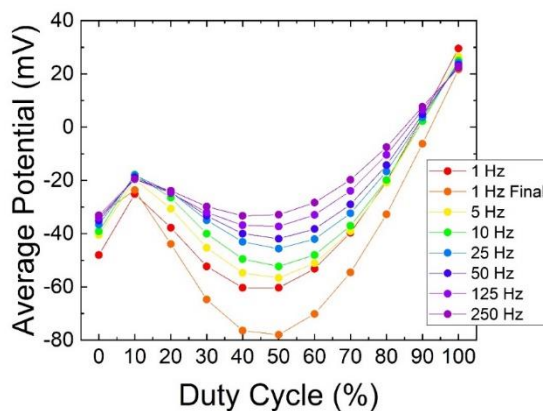


Figure S16: the output voltage as a function of the duty cycle for an RBIP with partially blocked pores. The sample and input signal parameters are as in Figure 2, the solution is 1mM HCl.

RBIP simulation

To estimate the ratchet-induced voltage between the two Ag/AgCl wires we assume that the voltages between the RBIP contacts and the Ag/AgCl wires next to them (V_L and V_R) can be modeled as charging and discharging capacitors. Figure S17a shows an illustration of the system and an equivalent circuit describing its operation.

The resting potential difference between each of the ratchet contacts and the wire next to it are $V_{R,eq}$ and $V_{L,eq}$, where subscript L,R denote left and right in Figure 1a and Figure S17a. In equilibrium $V_L = V_{L,eq}$ and $V_R = V_{R,eq}$. Since the ratchet is floating with respect to the wires, when a bias V_a is applied, one side of the ratchet is charged and the other is discharged. However, the bias is not necessarily shared equally between the two sides. We assign the parameter a to describe this source of asymmetry (yet, in all the subsequent results we assume that the charging is symmetric, i.e., $a=0.5$). If the input signal has a very long temporal period compared to the time constants for charging and discharging, the voltages in the system will reach their steady state values. For the first part of the period, the steady state voltages V_{Lf} and V_{Rf} are:

$$V_L = V_{Lf,1} = V_{L,eq} - aV_a; \quad V_R = V_{Rf,1} = V_{R,eq} + (1 - a)V_a \quad (s1)$$

We use subscript 1 to denote the first part of the temporal period ($t < d_c T$) where d_c is the duty cycle and T is the signal period. The second part of the period ($t > d_c T$), is noted with subscript 2. In this case the steady state voltages follow:

$$V_L = V_{Lf,2} = V_{L,eq} + (1 - a)V_a; \quad V_R = V_{Rf,2} = V_{R,eq} - aV_a \quad (s2)$$

According to the definitions in the Figure 1a, the output voltage V_{out} follows:

$$V_{out} = V_L + V_{in} - V_R \quad (s3)$$

In steady state conditions for a positive voltage applied on the ratchet

$$V_{out} = V_{L,eq} - aV_a + V_a - V_{R,eq} - (1 - a)V_a = V_{L,eq} - V_{R,eq} = \Delta V_{eq} \quad (s4)$$

Thus, in steady state conditions, the application of a constant bias does not drive the device away from its equilibrium voltage. Furthermore, in a perfectly symmetric system, the equilibrium voltages for the two surfaces are the same and the steady state output voltage will be 0.

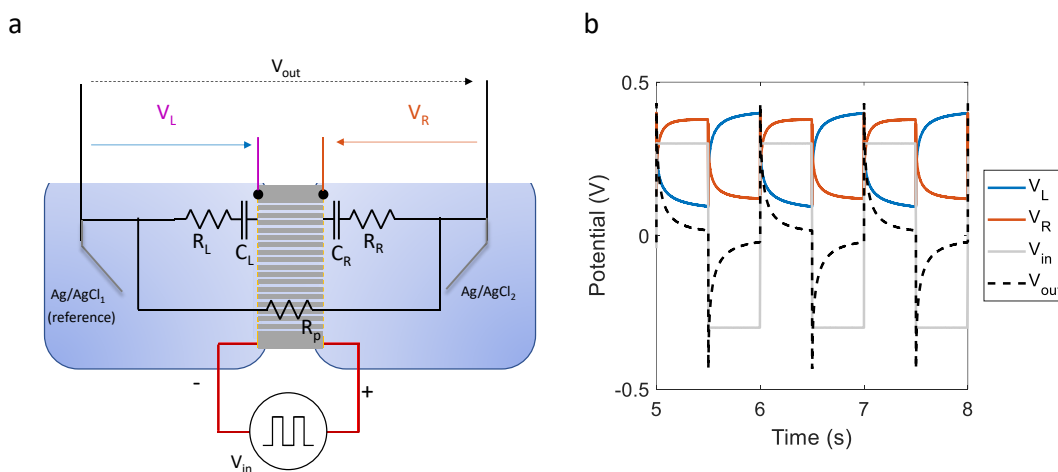


Figure S17: (a) an illustration of the ratchet setup with all the measured signals and equivalent circuit. (b) The measured voltages during ratchet operation. The frequency is 1 Hz, the duty cycle is 0.5 and the amplitude is $V_a = 0.3$ V.

Figure S17b shows an example of signals measured in response to an input signal with a 0.5 duty cycle, a frequency of 1 Hz, and an amplitude of $V_a = 0.3$ V. The voltage signals V_L and V_R can be approximately described by single exponent charging function defined by their initial voltage V_i , its time constant, τ , and the steady state voltage, V_f :

$$V(V_i, V_f, \tau, t) = V_f + (V_i - V_f) \exp\left(-\frac{t}{\tau}\right) \quad (\text{s5})$$

In non-linear systems such as double layers, the time constant is potential, frequency, and duty cycle dependent. The acceptable exponential fit to our experimental data (Figure 1, Figures S2-4) suggests that that for our RBIPs, the potential dependency can be described through the different time constants for charging and discharging the contacts. Thus, for a given frequency and duty cycle the transients will be determined by two time constants $\tau_1(d_c, f)$ and $\tau_2(d_c, f)$.

In the first part of every period, the input voltage is V_a . Thus, V_L discharges towards $V_{Lf,1}$ with a time constant of $\tau_{L,1}$:

$$\begin{aligned} V_{L,1}(t) &= V_{Lf,1} + (V_{Li,1} - V_{Lf,1}) \exp\left(-\frac{t}{\tau_{L,1}}\right) \\ &= V_{L,eq} - aV_a + (V_{Li,1} - V_{L,eq} + aV_a) \exp\left(-\frac{t}{\tau_{L,1}}\right) \end{aligned} \quad (\text{s6})$$

V_R charges towards $V_{Rf,1}$:

$$\begin{aligned} V_{R,1}(t) &= V_{Rf,1} + (V_{Ri,1} - V_{Rf,1}) \exp\left(-\frac{t}{\tau_{R,1}}\right) \\ &= V_{R,eq} + (1 - a)V_a \\ &\quad + (V_{Ri,1} - V_{R,eq} - (1 - a)V_a) \exp\left(-\frac{t}{\tau_{R,1}}\right) \end{aligned} \quad (\text{s7})$$

$V_{Li,1}$ and $V_{Ri,1}$ are calculated assuming that the V_R and V_L are continuous, and that the system is operating periodically in steady state.

For the second part of every period, we get:

$$\begin{aligned} V_{L,2}(t) &= V_{Lf,2} + (V_{Li,2} - V_{Lf,2}) \exp\left(-\frac{t - d_c T}{\tau_{L,2}}\right) \\ &= V_{L,eq} + (1 - a)V_a \\ &\quad + (V_{Li,2} - V_{L,eq} - (1 - a)V_a) \exp\left(-\frac{t - d_c T}{\tau_{L,2}}\right) \end{aligned} \quad (\text{s8})$$

And:

$$\begin{aligned} V_{R,2}(t) &= V_{Rf,2} + (V_{Ri,2} - V_{Rf,2}) \exp\left(-\frac{t - d_c T}{\tau_{R,2}}\right) \\ &= V_{R,eq} - aV_a + (V_{Ri,2} - V_{R,eq} + aV_a) \exp\left(-\frac{t - d_c T}{\tau_{R,2}}\right) \end{aligned} \quad (\text{s9})$$

Periodicity implies that:

$$V_{L,1}(t = 0) = V_{L,2}(t = T) \quad (\text{s10})$$

$$V_{L,1}(t = d_c T) = V_{L,2}(t = d_c T)$$

Inserting and noting $A_L = \exp\left(-\frac{d_c T}{\tau_{L,1}}\right)$, $B_L = \exp\left(-\frac{(1-d_c)T}{\tau_{L,2}}\right)$:

$$\begin{aligned} V_{Li,1} &= V_{Lf,2} + (V_{Li,2} - V_{Lf,2}) \exp\left(-\frac{T(1-d_c)}{\tau_{L,2}}\right) = V_{Lf,2} + (V_{Li,2} - V_{Lf,2})B_L \\ V_{Li,2} &= V_{Lf,1} + (V_{Li,1} - V_{Lf,1}) \exp\left(-\frac{Td_c}{\tau_{L,1}}\right) = V_{Lf,1} + (V_{Li,1} - V_{Lf,1})A_L \end{aligned} \quad (s11)$$

Inserting one into the other and extracting $V_{Li,2}$:

$$V_{Li,2} = \frac{V_{Lf,1} + (V_{Lf,2} - V_{Lf,1})A_L - B_L A_L V_{Lf,2}}{1 - B_L A_L} \quad (s12)$$

Similarly for V_R :

$$\begin{aligned} V_{R,1}(t = 0) &= V_{R,2}(t = T) \\ V_{R,1}(t = d_c T) &= V_{R,2}(t = d_c T) \end{aligned} \quad (s13)$$

Noting $A_R = \exp\left(-\frac{d_c T}{\tau_{r,1}}\right)$, $B_R = \exp\left(-\frac{(1-d_c)T}{\tau_{r,2}}\right)$:

We obtain:

$$V_{Ri,2} = \frac{V_{Rf,1} + (V_{Rf,2} - V_{Rf,1})A_R - B_R A_R V_{Rf,2}}{1 - B_R A_R} \quad (s14)$$

We can now find the output voltage at each stage:

$$V_{out} = V_L + V_{in} - V_R \quad (s15)$$

Inserting:

$$\begin{aligned} V_{out,1} &= V_{L,eq} - aV_a + (V_{Li,1} - V_{L,eq} + aV_a) \exp\left(-\frac{t}{\tau_{L,1}}\right) + V_a \\ &\quad - \left[V_{Re,q} + (1-a)V_a \right. \\ &\quad \left. + (V_{Ri,1} - V_{R,eq} - (1-a)V_a) \exp\left(-\frac{t}{\tau_{R,1}}\right) \right] \end{aligned} \quad (s16)$$

Rearranging:

$$\begin{aligned}
V_{out,1} &= (V_{L,eq} - V_{R,eq}) + (V_{Li,1} - V_{Leq} + aV_a) \exp\left(-\frac{t}{\tau_{L,1}}\right) \\
&\quad - (V_{Ri,1} - V_{Req} - (1-a)V_a) \exp\left(-\frac{t}{\tau_{R,1}}\right) \\
&= \Delta V_{eq} + (V_{Li,1} - V_{Lf,1}) \exp\left(-\frac{t}{\tau_{L,1}}\right) \\
&\quad - (V_{Ri,1} - V_{Rf,1}) \exp\left(-\frac{t}{\tau_{R,1}}\right)
\end{aligned} \tag{s17}$$

And for the second part of the period:

$$\begin{aligned}
V_{out,2} &= V_{L,eq} + (1-a)V_a + (V_{Li,1} - V_{Leq} - (1-a)V_a) \exp\left(-\frac{t-d_cT}{\tau_{L,2}}\right) - V_a \\
&\quad - \left[V_{R,eq} - aV_a + (V_{Ri,1} - V_{R,eq} + aV_a) \exp\left(-\frac{t-d_cT}{\tau_{R,2}}\right) \right]
\end{aligned} \tag{s18}$$

Rearranging:

$$\begin{aligned}
V_{out,2} &= V_{L,eq} - V_{R,eq} + (V_{Li,1} - V_{Leq} - (1-a)V_a) \exp\left(-\frac{t-d_cT}{\tau_{L,2}}\right) \\
&\quad - \left[(V_{Ri,1} - V_{R,eq} + aV_a) \exp\left(-\frac{t-d_cT}{\tau_{R,2}}\right) \right] \\
&= \Delta V_{eq} + (V_{Li,2} - V_{Lf,2}) \exp\left(-\frac{t-d_cT}{\tau_{L,2}}\right) \\
&\quad - (V_{Ri,2} - V_{Rf,2}) \exp\left(-\frac{t-d_cT}{\tau_{R,2}}\right)
\end{aligned} \tag{s19}$$

From equations (s17) and (s19) we can see that the net voltage is a result of the difference between the charging and the discharging of the two surfaces over the course of one period.

The time averaged voltage is found by the integrating V_{out} :

$$\begin{aligned}
\bar{V}_{out} &= \frac{1}{d_cT} \int_0^{d_cT} V_{out,1} dt + \frac{1}{(1-d_c)T} \int_{d_cT}^T V_{out,2} dt = \\
&= \Delta V_{eq} \\
&\quad + \frac{1}{d_cT} \left[\tau_{L,1} (V_{Li,1} - V_{Lf,1}) \left[1 - \exp\left(-\frac{d_cT}{\tau_{L,1}}\right) \right] \right. \\
&\quad \left. - \tau_{R,1} (V_{Ri,1} - V_{Rf,1}) \left[1 - \exp\left(-\frac{d_cT}{\tau_{R,1}}\right) \right] \right] \\
&\quad + \frac{1}{(1-d_c)T} \left[\tau_{L,2} (V_{Li,2} - V_{Lf,2}) \left[1 - \exp\left(-\frac{(1-d_c)T}{\tau_{L,2}}\right) \right] \right. \\
&\quad \left. - \tau_{R,2} (V_{Ri,2} - V_{Rf,2}) \left[1 - \exp\left(-\frac{(1-d_c)T}{\tau_{R,2}}\right) \right] \right]
\end{aligned} \tag{S20}$$

It can be easily shown that in a linear system where $\tau_{L,1} = \tau_{L,2}$ and $\tau_{R,1} = \tau_{R,2}$ the output is 0. However, if the capacitances are nonlinear such that the time constants are different, non-zero values for \bar{V}_{out} can be obtained. If the time constants are only determined by the duration of the two portions of the input signal (as demonstrated experimentally), then $\tau_{L,2} = \tau_{R,2}$ and $\tau_{L,1} = \tau_{R,1}$. In all the results presented here we have assumed that the RBIP is symmetric in the sense that ΔV_{eq} is 0 V, and a is 0.5.

References

1. Hänggi, P. & Marchesoni, F. Artificial Brownian motors: Controlling transport on the nanoscale. *Rev. Mod. Phys.* **81**, 387–442 (2009).
2. Reimann, P. Brownian motors: Noisy transport far from equilibrium. *Phys. Rep.* **361**, 57–265 (2002).
3. Siwy, Z. & Fuliński, A. A nanodevice for rectification and pumping ions. *Am. J. Phys.* **72**, 567–574 (2004).
4. Siwy, Z. & Fuliński, A. Fabrication of a Synthetic Nanopore Ion Pump. *Phys. Rev. Lett.* **89**, 4–7 (2002).
5. Kedem, O., Lau, B. & Weiss, E. A. How to Drive a Flashing Electron Ratchet to Maximize Current. *Nano Lett.* **17**, 5848–5854 (2017).
6. Kedem, O., Lau, B., Ratner, M. A. & Weiss, E. A. Light-responsive organic flashing electron ratchet. *Proc. Natl. Acad. Sci.* **114**, 8698–8703 (2017).
7. Kedem, O., Lau, B. & Weiss, E. A. How to Drive a Flashing Electron Ratchet to Maximize Current. *Nano Lett.* **17**, 5848–5854 (2017).
8. Roeling, E. M. *et al.* Organic electronic ratchets doing work. *Nat. Mater.* **10**, 51–55 (2011).